Structural basis of Rho-dependent transcription termination

Vadim Molodtsov[1,*], **Chengyuan Wang**[1,*,**], **Emre Firlar**[2], **Jason T. Kaelber**[2], **Richard H. Ebright**[1,**]

[1]Waksman Institute and Department of Chemistry and Chemical Biology, Rutgers University, Piscataway, NJ 08854, USA

[2]Rutgers CryoEM and Nanoimaging Facility and Institute for Quantitative Biomedicine, Rutgers University, Piscataway, NJ 08854, USA

Abstract

The ring-shaped hexameric ATP-dependent molecular motor Rho and the transcription elongation factor NusG mediate factor-dependent transcription termination and transcription-translation-coupling quality control in *Escherichia coli*[1–4]. Here, we report preparation of complexes functional in factor-dependent transcription termination from Rho, NusG, RNA polymerase (RNAP), and synthetic nucleic-acid scaffolds, and we report cryo-EM structures of complexes. The structures show that functional factor-dependent pre-termination complexes contain a closed-ring Rho hexamer, have RNA threaded through the central channel of Rho, have 60 nt of RNA interacting sequence-specifically with the exterior of Rho and 6 nt of RNA interacting sequence-specifically with the central channel of Rho, have Rho oriented relative to RNAP such that ATP-dependent translocation by Rho exerts mechanical force on RNAP, and have NusG bridging Rho and RNAP. The results explain five decades of research on Rho and provide a foundation for understanding Rho function.

One sentence summary

Cryo-EM reveals the structure of the functional Rho pre-termination complex

Five decades of genetic and biochemical experiments indicate that Rho-dependent transcription termination involves four steps (Fig. 1a)[1–23]. In the first step, the Rho hexamer in an open-ring state binds to RNA emerging from a transcription elongation complex (TEC), recognizing a long C-rich RNA sequence (Rho utilization site, *rut* site) through a primary binding site (PBS) on the exterior of the Rho hexamer (Fig. 1a, first image). In the second step, the Rho hexamer in the open-ring state recognizes a short pyrimidine-rich RNA sequence through a secondary binding site (SBS) in the central channel of the Rho hexamer

(Fig. 1a, second image). In the third step, the Rho hexamer transitions from the catalytically inactive, open-ring state to a catalytically competent, closed-ring state, with RNA threaded through the central channel of the Rho hexamer; this reaction is facilitated by interaction with NusG (Fig. 1a, third image). In the fourth step, the Rho hexamer in the catalytically competent, closed-ring state performs ATP-dependent 5'→3' translocation on RNA toward the TEC, exerting mechanical force on, and disrupting, the TEC (Fig. 1a, fourth image).

Four decades of genetic and biochemical experiments indicate that Rho mediates transcription-translation-coupling quality control by performing termination when, and only when, transcription-translation coupling is not occurring[1–4,24–29].

Recently, two research teams reported cryo-EM structures of Rho-TEC complexes[30–32]. However, the structures differed from expectation based on genetic and biochemical experiments in crucial respects[4,30–32]. The structures did not show the expected, catalytically competent, closed-ring state of Rho, the expected protein-RNA interactions with the Rho PBS and Rho SBS, the expected threading of RNA through Rho, the expected orientation of Rho relative to the TEC, and the expected interaction between Rho and NusG. A particularly striking difference from expectation was the orientation of Rho relative to the TEC. In the structures, the open-ring Rho hexamer was oriented with its N-terminal PBS domains directed toward the TEC, and its C-terminal ATPase domains directed away from the TEC; this orientation is *opposite* the expected orientation and is incompatible with ATP-dependent 5'→3' translocation on RNA toward the TEC.

The structures of *30* and *31* do not to correspond to any of the four functional states in the pathway of Rho-dependent termination expected based on the literature (Fig. 1a)[1–4,30–32]. The authors argue that Rho-dependent termination proceeds through a mechanism that "dramatically deviates from the textbook paradigm": namely, a mechanism that does not involve the ATP-dependent molecular-motor activity of Rho[31–33]. However, the stark discrepancy between the structures and previous results raises questions whether the structures represent *bona fide*, on-pathway, functionally relevant, states.

One specific basis for concern about the structures of *30* and *31* is that they were determined using complexes that had not been demonstrated to be functional in Rho-dependent termination.

Here, we have developed nucleic-acid-scaffold assays for Rho-dependent termination (Fig. 1b; Extended data Figs. 1–2), we have used the assays to identify scaffold sequences and reaction conditions that enable assembly of complexes functional in Rho-dependent termination (Fig. 1B; Extended data Figs. 1–2), and, then, we employed those sequences and conditions to prepare complexes and to determine structures by use of cryo-EM (Fig. 2; Extended data Figs. 3–5; Extended data Table 1; Supplementary Table 1). The resulting structures, in contrast to the structures of *30* and *31*, agree with--and account for--expectation from genetic and biochemical experiments (Figs. 2–4; Extended data Figs. 6–10).

Assembly of functional complexes

We prepared synthetic nucleic-acid scaffolds that comprised: (i) DNA and RNA determinants that direct formation of a TEC upon interaction with RNAP; (ii) a U-rich 5' extension of the RNA, of length 4, 5, 6, 7, 8, or 9 codons, to serve as an SBS ligand and as a "spacer" between SBS ligand and TEC; and (iii) a second RNA oligomer, provided *in trans*, containing a PBS ligand, either the natural λtR1 *rut* site[6] or the synthetic mimic dC75[22] (Fig. 1b, left). Using these scaffolds, we are able to demonstrate functional, efficient Rho-dependent transcription termination (Fig. 1b, right; Extended data Figs. 1–2). The activity depends on Rho, depends on PBS ligand, depends on NusG--and cannot be substituted by NusG N-terminal domain (NusG-N), which interacts with RNAP but not with Rho[1–4,26–28]-- and depends on ATP (Fig. 1b, right). Both the λtR1 *rut* site provided *in trans* and dC75 provided *in trans* supported activity (Fig. 1; Extended data Fig. 1); shorter PBS ligands (dC5 and dC15) did not support efficient Rho-dependent termination, consistent with their previously demonstrated weaker interactions with Rho[21] (Extended data Fig. 1). Equivalent results were obtained using 5' U-rich extensions of the RNA of lengths 4, 5, 6, 7, 8, and 9 codons (Extended data Fig. 2a). Equivalent results were obtained using scaffolds having fully complementary DNA nontemplate and template strands (Extended data Fig. 1a) and nucleic-acid scaffolds having a partially noncomplementary sequence corresponding to the nontemplate strand of the transcription bubble (Extended data Fig. 1b). Equivalent results were obtained using RNA-release assays, in which Rho-dependent termination is assessed by detection of RNA released from immobilized TECs (Fig. 1; Extended data Fig. 1), and using RNA-extension assays, in which Rho-dependent termination is detected by cessation of RNA extension (Extended data Fig. 2).

Structures of functional complexes

Having identified sequences and conditions that enable preparation of complexes proficient in Rho-dependent termination, we prepared complexes, we trapped complexes in a state poised to perform ATP-dependent Rho translocation by replacing ATP by the ATP analog Mg-ADP-BeF$_3$[22–23], and we determined structures by use of single-particle-reconstruction cryo-EM (Fig. 2; Extended data Figs. 2–5). We determined three sets of structures: (i) a structure containing λtR1 *rut* as PBS ligand, Rho, NusG, and TEC (λtR1-Rho-NusG-TEC; n = 6; 4.3 Å resolution), (ii) a structure containing dC75 as PBS ligand, Rho, NusG, and TEC (dC75-Rho-NusG-TEC; 4.1 Å resolution), and (iii) structures containing only Rho, NusG, and TEC (Rho-NusG-TEC; 4.2–6.5 Å resolution) (Fig. 2; Extended data Figs. 3–5).

The resulting structures differ radically from the structures of *30* and *31*. In λtR1-Rho-NusG-TEC and dC75-Rho-NusG-TEC, Rho adopts a catalytically competent, closed-ring state, superimposable on the catalytically competent, closed-ring state observed in crystal structures of Rho bound to Mg-ADP-BeF$_3$ in the absence of a TEC[21–23] (Fig. 2a–b), in contrast to the structures of *30* and *31*, in which Rho adopts a catalytically incompetent, open-ring conformation (Fig. 2; Extended data Fig. 6). Comparison of λtR1-Rho-NusG-TEC and dC75-Rho-NusG-TEC structures to the structures of *30* and *31* indicates that the Rho hexamer is rotated by ~150° about one axis, essentially flipping its orientation relative

to the TEC, is rotated by ~40° about a second axis, and is translated by ~60–70 Å (Extended data Fig. 6).

In λtR1-Rho-NusG-TEC and dC75-Rho-NusG-TEC, the central channel of the closed-ring Rho hexamer is aligned with the TEC RNA exit channel, and the closed-ring Rho hexamer is located immediately at the mouth of the TEC RNA exit channel, such that RNA proceeds directly from the TEC into, and through, the Rho hexamer (Fig. 2a–b), enabling interactions of the U-rich SBS ligand with the Rho SBS site (Fig. 2a–b), and interactions of the RNA oligomer, provided *in trans*, serving as PBS ligand, with the N-terminal domains of the six protomers of the Rho hexamer (Fig. 2a–b). In λtR1-Rho-NusG-TEC and dC75-Rho-NusG-TEC, Rho is oriented with its C-terminal ATPase domains toward the TEC and its N-terminal PBS domains away from the TEC, and thus, is in the orientation that enables ATP-hydrolysis-dependent translocation toward the TEC (Fig. 2a–b). Crucially, in our structures, NusG bridges the TEC and Rho, with NusG-N interacting with RNAP and NusG-C interacting with Rho (Fig. 2a–b).

In the crystal structure of a catalytically competent, closed-ring state of Rho bound to an SBS ligand and Mg-ADP-BeF$_3$ in the absence of NusG and TEC, the six Rho protomers exhibit differences in spacing, conformation, interactions, and occupancy levels of Mg-ADP-BeF$_3$, corresponding to differences in motor state, and were assigned as protomers A-F[4,22]. In our structures, the six Rho protomers exhibit the same differences in spacing, conformation, interactions, and occupancy levels of Mg-ADP-BeF$_3$, and thus can be assigned in the same manner as protomers A-F (Fig. 2a–b, right). In our structures, Rho is oriented relative to the TEC such that NusG-C interacts with the Rho protomers designated B and C (Fig. 2a–b, right).

The complex not having a PBS ligand, Rho-NusG-TEC, has the same overall structural organization as the complexes having a PBS ligand (Fig. 2c vs. Fig. 2a–b; Extended data Fig. 5). This finding, together with our finding that the PBS ligand is required for Rho-dependent termination with our sequences and conditions (Fig. 1b, right; Extended data Figs. 1–2), implies that, under our conditions, the PBS ligand is not essential for assembly of the Rho-NusG-TEC complex, but is essential for subsequent steps in Rho-dependent termination. We hypothesize, consistent with previous data[21], that the PBS ligand facilitates Rho-dependent termination allosterically, by inducing a conformational or dynamic state of Rho competent for ATP-dependent translocation. The lower map quality, especially for Rho, in our structures of complex without a PBS ligand precludes defining details of the PBS-ligand-dependent change in conformation or dynamics, but is consistent with a PBS-ligand-dependent decrease in dynamics.

Protein-RNA interactions

In our structures of λtR1-Rho-NusG-TEC and dC75-Rho-NusG-TEC, we observe unambiguous density for 85-88 nt of RNA, comprising 14 nt interacting with the TEC, 7 nt in the spacer between the TEC and the Rho SBS, 6 nt of SBS-ligand RNA interacting with the Rho SBS, and 58-61 nt of PBS-ligand RNA interacting with the Rho PBS (58 nt in λtR1-Rho-NusG-TEC; 61 nt in dC75-Rho-NusG-TEC; Fig. 3; Extended data Figs. 3–4).

As such, the structures provide a *complete* description of protein-RNA interactions in the complexes.

The structures of λtR1-Rho-NusG-TEC and dC75-Rho-NusG-TEC reveal the full interactions of the PBS ligand with the Rho hexamer (Fig. 3a). All six protomers of the Rho hexamer interact with PBS-ligand RNA. Rho protomer B--one of the two protomers that interacts with NusG-C--interacts with the 5' end of the PBS ligand, and Rho protomer A interacts with the 3' end of the PBS ligand (Fig. 3a, top). Ten nucleotides of PBS-ligand RNA are associated with each Rho protomer; 5 nt of the PBS ligand make potentially sequence-specific interactions with α-helix 4 and β strands 4-5 of the Rho protomer (Fig 3a, top, red), and 5 nt of the PBS ligand connect the sequence-specifically recognized RNA segment associated with one Rho protomer with the sequence-specifically recognized RNA segment associated with the next Rho protomer (Fig 3a, top, green). The observed interactions are essentially identical for λtR1-Rho-NusG-TEC and dC75-Rho-NusG-TEC (Fig. 3a, top; Extended data Fig. 7a). The interactions by 2 nt of the 10 nt of PBS ligand associated with each Rho protomer are superimposable on interactions observed in a crystal structure of having a Rho hexamer interacting with six copies of a 2 nt RNA oligomer in the absence of NusG and TEC[17] (Extended data Fig. 7b). The interactions of the other 8 nt of the 10 nt of PBS ligand associated with each Rho protomer were not previously defined. In the structures of *30*, interactions between the PBS ligand and Rho were limited to just one of the six Rho protomers (Extended data Fig. 7c), and in the structures of *31*, interactions between the PBS ligand and Rho were absent (Extended data Fig. 7d). Indeed, in the structures, of *30* and *31*, structural elements of RNAP and template-strand DNA interact with the PBS of three to four Rho protomers, sterically precluding interactions of the PBS ligand with those Rho protomers (Extended data Fig. 7c–d).

Our finding that each Rho protomer interacts with 10 nt of the PBS-ligand RNA enables us to divide the PBS ligand into six 10 nt segments, to align the six 10 nt segments to derive a consensus PBS-ligand sequence for Rho protomer interaction (AAACCCAAUC; Fig. 3a, bottom left), and, by concatenating six copies of that sequence, to derive a consensus PBS-ligand sequence for Rho hexamer interaction ([AAACCCAAUC]$_6$; Fig. 3a, bottom left). We have synthesized the consensus PBS ligand for Rho hexamer interaction, and we have shown that it supports efficient Rho-dependent transcription termination (Fig. 3a, bottom right), indicating that the consensus PBS ligand is a functional PBS ligand. Our consensus PBS-ligand sequence defines a structure-based functional length (60 nt) and a structure-based functional sequence ([AAACCCAAUC]$_6$) for the PBS ligand, significantly advancing the understanding of the sequence requirements for a PBS ligand (previously essentially limited to the requirement for a ~50-80 nt sequence rich in C and poor in G[1–4,9]).

Six nucleotides of SBS-ligand RNA make tight interactions with the central channel of the closed-ring Rho hexamer (Fig. 3b), in a manner superimposable on interactions observed in a crystal structure of a Rho hexamer interacting with SBS-ligand RNA in the absence of NusG and TEC[22]. The 6 nt of SBS-ligand RNA form a right-handed helix (Fig. 3b). Interactions with this right-handed helix are made by the Q and R-loops of Rho protomers A-E, which protrude from the Rho C-terminal ATPase domain into the central channel of the Rho hexamer, and which are arrayed in a right-handed spiral that tracks the right-handed

helix formed by SBS-ligand RNA (Fig. 3b). Rho protomer A interacts with nucleotides at the 5' end of the SBS ligand; Rho protomers B, C, D, and E interact with successive nucleotides of the SBS ligand ordered in the direction 5'→3'; and Rho protomer F makes no interaction with SBS ligand (Fig 3b).

RNA within the TEC RNA-exit channel connects to the SBS ligand through a 7 nt spacer RNA (Fig. 3c). The spacer RNA passes through a wide portion of the central channel of the Rho hexamer and makes no interactions with Rho (Fig. 3c). The 2 nt of the spacer RNA closest to the TEC RNA-exit channel interact with residues of the RNAP β'-subunit zinc-binding domain (ZBD; Fig. 3c), these interactions with the ZBD are distinctive and are not observed in structures of TECs without additional factors[33] or in structures of functional transcription-translation complexes[34–35].

In our work we used a discontinuous RNA, with the PBS ligand provided *in trans* and the remaining RNA provided *in cis*. Model building based on our structures indicates that the 3' end of the PBS ligand can be connected to the 5' end of the SBS ligand through an RNA connector having a minimum length of 10-11 nt. Model building further suggests that there is freedom for bulging, looping, and/or secondary-structure formation in the RNA connector between the 3' end of the PBS ligand and the 5' end of the SBS ligand, and thus suggests the connector could accommodate longer lengths of RNA.

Protein-protein interactions

The interface between the NusG-containing TEC and Rho in λtR1-Rho-NusG-TEC and dC75-Rho-NusG-TEC involves three protein-protein interactions: a protein-protein interaction by NusG-C (498 Å^2 buried surface area), and smaller interactions between the RNAP β-subunit flap-tip helix (FTH; 245 Å^2 buried surface area) and the RNAP ω subunit (158 Å^2 buried surface area; Fig. 4a).

In our structures, NusG bridges RNAP and Rho (Figs 2, 4a–b), NusG-N interacts with its known binding site on RNAP[36], NusG-C interacts with Rho protomers B and C, and NusG-N is connected to NusG-C through a partly flexible linker (NusG linker; Figs. 2, 4a–b; Extended data Fig. 8a). In our structures of λtR1-Rho-NusG-TEC and dC75-Rho-NusG-TEC, there is unambiguous density for NusG-N, NusG-C, and the NusG linker (Extended data Figs. 3g, 4g). NusG-C wedges between the C-terminal ATPase domains of Rho protomer B and Rho protomer C (Figs. 2, 4a–b; Extended data Fig. 8a). NusG-C interacts extensively with the ATPase domain of Rho protomer C (388 Å^2 buried surface area); the interaction involves the β7-β8 loop and β9-β10 loop of NusG and α-helices 16 and 18 of Rho protomer C (Fig. 4B, right; Extended data Fig. 8a). NusG makes a second interaction with the ATPase domain of Rho protomer B (110 Å^2 buried surface area); this interaction involves the β8-β9 loop and β10-β11 loop of NusG-C and α-helix 17 of Rho protomer B (Fig. 4b, left; Extended data Fig. 8a). The interaction between NusG-C and Rho protomer C matches the interaction reported for a crystal structure of a Rho hexamer bound to six copies of a NusG-C protein fragment, with each of the six Rho protomers interacting with one copy of NusG-C protein fragment[23] (Extended data Fig. 8b). The interaction between NusG-C and Rho protomer B was not previously known.

It previously has been shown that interaction of NusG-C with Rho facilitates formation of the catalytically competent, closed-ring state of the Rho hexamer[1–4,23]. Our structures reveal three additional functions of the interactions involving NusG. First, by bridging the TEC and Rho, NusG stabilizes the TEC-Rho interface (Figs. 2, 4a–b). Second, by interacting with Rho protomers B and C, NusG sets the rotational orientation of the Rho hexamer relative to the TEC (Figs. 2–3; Extended data Fig. 8b), and thus sets the initial motor state of the Rho hexamer (Fig. 4e). One of the two Rho protomers that interacts with NusG, protomer B, serves as the binding site for the 5' end of the PBS ligand and thus as the probable point of initial interaction between the PBS ligand and Rho (Fig. 3a); the two protomers of Rho that interact with NusG, protomers B and C, make the most highly ordered interactions with the SBS ligand (Fig. 3b, right); and the protomer of Rho that makes the most extensive interaction with NusG-C, protomer C, interacts with the crucial central position of the SBS ligand (Fig. 3b, right). The ATP binding site between the two protomers of Rho that interact with NusG, protomers B and C, is one of the two ATP binding sites that exhibit highest occupancy and order of Mg-ADP-BeF$_3$ and associated protein segments (Extended data Fig. 9) and is the one ATP binding site that exhibits occupancy, order, and geometry that indicate it is fully poised for ATP hydrolysis (motor state T*2[4,22]; Fig. 4e; Extended data Fig. 9). Third, and probably most important, by wedging between Rho protomers B and C, NusG constrains the rotational orientation of the Rho hexamer relative to the TEC (Figs. 2–3; Extended data Fig. 8b), preventing rotation of the Rho hexamer relative to the TEC during ATP hydrolysis by Rho, thereby preventing futile cycles of ATP-dependent rotation of Rho relative to the TEC and enforcing functional cycles of ATP-dependent translocation of Rho relative to the TEC. NusG thus serves as a *stator* for the Rho-NusG-TEC motor complex, analogous, in all respects, to the stator formed by the *b* subunit of the F$_1$F$_0$ ATP synthase/ATPase motor complex[37].

The other protein-protein interactions at the Rho-TEC interface are: (i) an interaction between the RNAP β-subunit FTH and Rho protomer B (Fig. 4c), and (ii) an interaction between the RNAP ω subunit and Rho protomer F (Fig. 4d). In the absence of NusG, or in the presence of a NusG derivative lacking NusG-C, Rho-dependent termination is dramatically reduced, but is not eliminated[1–4] (Extended data Fig. 1). We infer that, in the absence of NusG, or in the presence of a NusG derivative lacking NusG-C, protein-protein interactions by the RNAP β FTH and RNAP ω partly, but not completely, constrain rotational orientation of Rho relative to the TEC during ATP hydrolysis, and thus partly, but not completely, serve as the motor stator required for functional ATP-dependent translocation of Rho relative to the TEC.

Motor properties

Our structures, together with the ATPase cycle proposed for Rho[22], suggest the following mechanism for ATP-dependent translocation by Rho (Fig. 4e). In the first cycle of ATP-dependent translocation by Rho, ATP hydrolysis occurs at the ATP binding site at the interface between the Rho protomers contacted by NusG, protomers B and C (T*2; Fig 4e, left). This resets the motor state of the ATP binding site between Rho protomers B and C from the state fully poised for ATP hydrolysis (T*2) to the first state with ADP bound (D1) and increments the motor states of the other ATP binding sites by one state (Fig. 4e, left

vs. Fig. 4e, center). Concurrently, this results in relocation of the 5' nucleotide of the SBS ligand out of the Rho SBS (Fig. 4e, left, green filled circle vs. Fig. 4e, center, green open circle), relocation of the 3' nucleotide of the SBS ligand into the Rho SBS (Fig. 4e, left, green open circle vs. Fig. 4e, center, green filled circle), and relocation of the 5' nucleotide of the RNA spacer into the position previously occupied by the 3' nucleotide of the SBS ligand (Fig. 4e, center, brick-red open circle). The resulting translocation of Rho by 1 nt relative to the spacer RNA and the TEC applies mechanical force to the TEC, causing either forward translocation of the TEC by 1 nt without nucleotide addition (hypertranslocation model [1] [3–4,18]), extraction of RNA from the TEC by 1 nt (RNA-extraction model[1,3–4]), or reorganization of TEC structure (allosteric model[1,3–4,19]), and thereby inhibits RNA extension by the TEC and predisposes the TEC to dissociation. In the second cycle, hydrolysis occurs at the ATP binding site at the interface between Rho protomers C and D. This resets the motor state of the ATP binding site between Rho protomers C and D from T*2 to D1, increments the motor states of the other five ATP binding sites by one state (Fig. 4e, center vs. Fig. 4e, and right), and results in translocation of Rho by an additional 1 nt relative to the spacer RNA and the TEC, further applying mechanical force on the TEC, and thereby further inhibiting RNA extension by the TEC and further predisposing the TEC to dissociation (Fig. 4e, center and left). Subsequent cycles, carried out in the same manner, result in the further translocation by Rho relative to the spacer RNA and the TEC, further application of additional force to the TEC, and, ultimately, dissociation of the TEC.

Discussion

Our structures of λtR1-Rho-NusG-TEC and dC75-Rho-NusG-TEC agree, in all respects, with expectations from genetic and biochemical evidence results concerning Rho-dependent termination[1–24]. The structures show a catalytically competent, closed-ring conformation of Rho, show threading of RNA through the central channel of Rho, show the full PBS ligand interacting with the full Rho PBS, show the full SBS ligand interacting with the full Rho SBS, show Rho oriented relative to RNAP such that ATP-dependent translocation can occur and can apply mechanical force to the TEC, and show NusG bridging the TEC and Rho (Figs. 2–4). We conclude that λtR1-Rho-NusG-TEC and dC75-Rho-NusG-TEC define the structure of the third state in the "textbook" model, the state in which the complex is fully assembled and fully poised to begin ATP-dependent Rho translocation (Fig 1A, third subpanel). We designate this state the "Rho pre-termination complex," and we propose it is the state functionally responsible for all or most Rho-dependent transcription termination in *E. coli*. Following submission of our manuscript for publication, a preprint reported a cryo-EM structure of a *Thermus thermophilus* Rho-TEC complex--without PBS ligand and without NusG--that exhibits a closed-ring Rho hexamer, RNA threaded through Rho, and the same orientation of Rho relative to TEC as in our structures.[39] The preprint supports the conclusion that these features are defining features of functional Rho pre-termination complexes. As stated above, the structures of *30* and *31* lack these features and cannot be linked to any of the four states in the "textbook model" of Rho-dependent termination (Fig. 1a; Extended data Fig. 6). We suggest that the structures of *30* and *31* correspond to either: (i) states that precede the four states in the "textbook" model in Fig. 1a (e.g., "pre-loading" states that precede full interaction of Rho with RNA), (ii) states that function

only at specialized sequences or under specialized conditions, or (iii) off-pathway states that are non-functional and abiological.

Comparison of the structures of functional transcription-translation complexes (TTC-B[29,35–36]) and functional Rho pre-termination complexes (Figs. 2–4) establishes that the two sets of complexes are mutually exclusive (Extended data Fig. 10). The ribosome 30S subunit in TTC-B and Rho in the Rho pre-termination complex occupy the same face of the TEC; they cannot co-occupy without extensive steric overlap (Extended data Fig. 10). In addition, NusG bridges the ribosome 30S and the TEC in TTC-B, but bridges Rho and the TEC in the Rho pre-termination complex (Extended data Fig. 10). Comparison of the structures supports the following simple mechanism for Rho-dependent transcription-translation-coupling quality control[1–4,26–29]: When transcription-translation coupling is occurring, Rho is unable to form a Rho pre-termination complex and unable to terminate transcription; in contrast, when transcription-translation coupling is disrupted--for example, when the ribosome stalls but the TEC continues translocating downstream--Rho is able to form a Rho pre-termination complex and to terminate transcription. In this mechanism, both the TEC and NusG switch partners in the transition from transcription-translation-coupling to Rho-dependent termination. In transcription-translation coupling, the TEC makes interactions with the ribosome, and NusG makes interactions, mediated by NusG-C, with the ribosome[1–4, 26–29,35–36]. In contrast, in the Rho pre-termination complex, as discussed above, the TEC makes interactions with Rho, and NusG makes interaction, mediated by NusG-C, with Rho (Fig. 4a–d).

The structures presented in this work restore the "textbook" model for Rho-dependent termination and reveal the protein-RNA interactions, protein-protein interactions, and protein-motor properties of functional Rho pre-termination complexes. Key priorities for future work include determination of a structure of a Rho pre-termination complex containing a continuous RNA extending from the PBS ligand to the RNA 3' end (as opposed to the current complexes, in which the PBS ligand is provided *in trans*; Figs. 1b–3), determination of a structure of a complex having the consensus PBS-ligand sequence defined in this work (Fig. 3a), determination of a structure of a complex that includes the transcription elongation factor NusA, which can be present in both TECs and TTCs[1–4,29,36,38], and determination of structures of trapped intermediates after one, two, or more cycles of ATP-dependent Rho translocation (Fig. 4e). The structures of this work provide an essential foundation for understanding Rho-dependent transcription termination and a platform for further structure determination illuminating the final, ATP-dependent steps in Rho-dependent transcription termination.

Methods

E. coli RNAP core enzymes

E. coli RNAP core enzyme was prepared from *E. coli* strain BL21 Star (DE3) (ThermoFisher) transformed with plasmid pVS10 (encodes *E. coli* RNAP β' with C-terminal hexahistidine tag, β, α, and ω subunits)[39], as described[40]. The product (purity >99%) was stored in aliquots in RNAP storage buffer (10 mM Tris-HCl, pH 7.6, 100 mM NaCl, 0.1 mM EDTA, and 5 mM dithiothreitol) at −80°C.

E. coli NusG

E. coli NusG was prepared from *E. coli* strain BL21 Star (DE3) (ThermoFisher) transformed with plasmid pIA247 (encodes *E. coli* NusG with C-terminal hexahistidine tag)[41], as described[41]. The product (purity >95%) was stored in aliquots in RNAP storage buffer at −80°C.

E. coli NusG-N (NusG[1-123]) was prepared from *E. coli* strain BL21 Star (DE3) (ThermoFisher) transformed with plasmid pRM431-NusG-N [constructed by site-directed mutagenesis of plasmid pRM431 (encodes *E. coli* NusG with N-terminal hexahistidine tag)[23], using Vent DNA polymerase (New England Biolabs) and primers 5'-CAGCAGGTTGGTGATAAGCCGCGTTAGAAAACGCTGTTTGAACCGGGTGAAATGG-3' and 5'-CCATTTCACCCGGTTCAAACAGCGTTTTCTAACGCGGCTTATCACCAACCTGCTG-3'] as described for NusG. The product (purity >95%) was stored in aliquots in RNAP storage buffer at −80°C.

E. coli Rho

E. coli Rho was prepared from *E. coli* strain BL21 Star (DE3) (ThermoFisher) transformed with plasmid pET24b-Rho (encodes *E. coli* Rho)[16]. Cultures of transformants in 3 L LB broth[42] containing 30 μg/ml kanamycin were shaken at 37°C until OD_{600} = 0.7, were induced by addition of IPTG and additional shaking for 3 h to at 37°C 1 mM. Cells were harvested by centrifugation 10 min at 5,000xg at 4°C, re-suspended in lysis buffer [20 mM Tris-HCl, pH 7.6, 50 mM NaCl, 1 mM EDTA, 1 mM β-mercaptoethanol, and EDTA-free protease inhibitor cocktail (Sigma-Aldrich), and lysed by sonication [Sonifer 450 (Branson); 5 min; output setting 8; duty cycle 30%] on ice. The cell lysate was cleared by centrifugation 30 min at 20,000xg at 4°C, the cleared lysate was applied to a 5 ml HiTrap Q HP column (GE Healthcare) equilibrated with TGE[42] containing 50 mM NaCl and 1 mM β-mercaptoethanol, and the column was eluted with a gradient of 50-500 mM NaCl in 30 column volumes of the same buffer. Pooled fractions containing Rho (~300-400 mM NaCl) were concentrated to 2 ml by centrifugation 30 min at 4,000xg at 4°C through a 20 ml VivaSpin 20 30 kDa MWCO concentrator (Sartorius, and were diluted with TGE containing 1 mM β-mercaptoethanol to adjust the NaCl concentration to 50 mM. The resulting sample was applied to a 5 ml HiTrap HP heparin column (GE Healthcare) equilibrated with TGE containing 50 mM NaCl and 1 mM β-mercaptoethanol, and the column was eluted with a gradient of 50-700 mM NaCl in 40 column volumes of the same buffer. Pooled fractions containing Rho (~300-400 mM NaCl) were concentrated to 2 ml by centrifugation 30 min at 4,000xg at 4°C through a VivaSpin 20 30 kDa MWCO concentrator. The resulting sample was applied to a 120 ml HiLoad 16/60 Superdex 200 size-exclusion column (GE Healthcare) equilibrated with 10 mM Tris-HCl, pH 7.6, 100 mM NaCl, and 1 mM β-mercaptoethanol, and the column was eluted with one column volume of the same buffer. Fractions containing pure Rho were pooled and concentrated to 100 μM using a VivaSpin20 30 kDa MWCO concentrator. The product (purity >98%) was stored in aliquots at −80°C.

Nucleic acids

Oligodeoxyribonucleotides and oligoribonucleotides (sequences in Fig. 1b; Extended data Figs. 1–2) were purchased (Integrated DNA Technologies; PAGE-purified; nontemplate-strand oligodeoxyribonucleotides purchased in both non-biotinylated and 3'-biotinylated form), dissolved to 1 mM in 5 mM Tris-HCl, pH 7.5, and stored in aliquots at −80°C. Nucleic-acid scaffolds comprising nontemplate-strand DNA, template-strand DNA, and RNA product (sequences in Fig. 1b; Extended data Figs. 1–2) were prepared by mixing 60 μM nontemplate-strand oligodeoxyribonucleotide, 60 μM template-strand oligodeoxyribonucleotide, and 60 μM RNA-product oligoribonucleotide or 5'-^{32}P-labelled oligoribonucleotide [0.6 Bq/fmol; prepared by labelling of oligodeoxyribonucleotide using T4 polynucleotide kinase (New England BioLabs) and ATP or [γ^{32}P]-ATP (Perkin-Elmer) in 100 μl annealing buffer (5 mM Tris-HCl, pH 7.5), heating 10 min at 95°C, and cooling over 3 h to 22°C; the resulting nucleic-acid scaffolds were stored in aliquots at −80°C. Partial nucleic-acid scaffolds comprising template-strand DNA and RNA product were prepared in the same manner, but omitting nontemplate-strand oligodeoxyribonucleotide.

ADP-BeF$_3$

ADP-BeF$_3$ was prepared by reaction of 70 mM BeSO$_4$ (Sigma-Aldrich) and 350 mM NaF (Sigma-Aldrich) in 50 μl 2 mM Tris-HCl, pH 7.0 for 1 min at 22°C, followed by addition of 15 μl 100 mM ADP (Sigma-Aldrich). ADP-BeF$_3$ was prepared freshly for each sample and was kept on ice until used.

Scaffold assay for Rho-dependent transcription termination: RNA release

Reaction mixtures containing 0.5 μM RNAP core enzyme and 0.5 μM partial nucleic-acid scaffold comprising template-strand oligodeoxyribonucleotide and 5'–^{32}P-labelled RNA-product oligoribonucleotide (0.6 Bq/fmol) in 10 μl transcription buffer (20 mM Tris-HCl, pH 7.9, 10 mM MgCl$_2$, 20 mM KCl, and 1 mM DTT) were incubated 10 min at 22°C, were supplemented with 1 μl 6 μM 3'-biotinylated nontemplate-strand oligodeoxyribonucleotide and incubated 5 min at 22°C, were supplemented with 1 μl 0 or 30 μM NusG derivative (NusG or NusG-N) and incubated 5 min at 22°C, were supplemented with PBS-ligand oligoribonucleotide (1 μl 0 or 50 μM λtR1 *rut*, 1 μl 50 μM dC75, 1 μl 150 μM dC15, or 1 μl 750 μM dC5) and incubated 1 min at 22°C, and were supplemented with 1 μl 0 or 30 μM Rho and incubated 5 min at 22°C. The resulting complexes were bead-immobilized by adding 1 μl on streptavidin-coated agarose beads (Pierce Streptavidin Agarose; ThermoFisher; pre-washed with transcription buffer), incubating 10 min at 22°C, and removing unbound complex by washing with 3 x 100 μl of transcription buffer. The resulting immobilized complexes were supplemented with 1 μl 0 or 1 mM ATP (>99% purity; ThermoFisher) in transcription buffer and incubated 5 min at 37°C (to enable termination), were supplemented with 1 μl 400 μM UTP , 400 μM CTP, and 1 mM 3'-d-GTP [>99% purity for UTP and CTP (ThermoFisher);   95% purity for 3'-dGTP (Jena Bioscience)] and incubated 2 min at 37°C (to "chase," and thereby to stabilize, non-terminated complexes), and supernatants and beads were separated by centrifugation 1 min at 2,000xg at 22°C. Supernatant aliquots (10 μl) were removed and mixed with equal volumes of 2x stop buffer (90% formamide, 50 mM EDTA, 0.01% bromophenol

blue, and 0.01% xylene cyanole) at 22°C, and pellets (beads) were washed with 60 μl 1x stop buffer (45% formamide, 25 mM EDTA, 0.005% bromophenol blue, and 0.005 xylene cyanole) at 22°C. Reaction products in supernatant and pellet factions were resolved by electrophoresis on 7 M urea, 20% polyacrylamide gels (19:1 acrylamide: bis-acrylamide[42], were detected using storage-phosphor imaging (Typhoon PhosphorImager, GE Healthcare), and were quantified using ImageQuant 5.2 (GE Healthcare).

Scaffold assay for Rho-dependent transcription termination: RNA extension

Reaction mixtures) containing 0.5 μM RNAP core enzyme and 0.5 μM partial; nucleic-acid scaffold comprising template-strand oligodeoxyribonucleotide and 5'-^{32}P-labelled RNA-product oligoribonucleotide (0.6 Bq/fmol) in 10 μl transcription buffer were incubated 10 min at 22°C, were supplemented with 1 μl 6 μM nontemplate-strand oligodeoxyribonucleotide and incubated 5 min at 22°C, were supplemented with 1 μl 0 or 30 μM NusG derivative (NusG or NusG-N) and incubated 5 min at 22°C, were supplemented with PBS-ligand oligoribonucleotide (1 μl 0 or 50 μM λtR1 *rut*, 1 μl 50 μM dC75, 1 μl 150 μM dC15, or 1 μl 750 μM dC5) and incubated 1 min at 22°C, and were supplemented with 1 μl 0 or 30 μM Rho and incubated 5 min at 22°C. The resulting reaction mixtures then were supplemented with 1 μl 0 or 1 mM ATP (>99% purity; ThermoFisher) in transcription buffer and incubated 5 min at 37°C (to enable termination), were supplemented with 1 μl mM 400 μM UTP, 400 μM CTP, and 400 μM 3'-dGTP [>99% purity for UTP and CTP (ThermoFisher);   95% purity for 3'-dGTP (Jena Bioscience)] and incubated 2 min at 37°C (to "chase" non-terminated complexes), and were mixed with 10 μl 2x stop buffer at 22°C. Reaction products were resolved by electrophoresis on 7 M urea, 20% polyacrylamide gels (19:1 acrylamide: bis-acrylamide)[42], were detected using storage-phosphor imaging (Typhoon PhosphorImager, GE Healthcare), and were quantified using ImageQuant 5.2 (GE Healthcare).

Cryo-EM structure determination: sample preparation

Reaction mixtures containing 4 μM RNAP core enzyme and 5 μM nucleic-acid scaffold comprising nontemplate-strand DNA, template-strand DNA and RNA product in 100 μl transcription buffer were incubated 10 min at 22°C, were supplemented with 25 μl 30 μM NusG derivative and incubated 5 min at 22°C, were supplemented with 3 μl 0 or 1 mM PBS-ligand oligoribonucleotide (λtR1 *rut* or dC75) and incubated 1 min at 22°C, and were supplemented with 50 μl 60 μM Rho and 2 μl 24 mM ADP-BeF$_3$ and incubated 5 min at 22°C. The resulting complexes were concentrated to 35 μl (~12 μM final concentration) by centrifugation 12 min at 20,000xg at 4°C through pre-chilled Amicon Ultra-0.5 30K MWCO concentrators (EMD Millipore), supplemented with 4 μl of ice-cold 80 mM CHAPSO (Hampton Research), and kept on ice until applied to EM grids.

EM grids were prepared using a Vitrobot Mark IV autoplunger (FEI/ThermoFisher), with the environmental chamber set to 22°C and 100% relative humidity. Samples (3 μl) were applied to Quantifoil 1.2/1.3 Cu 300 holey-carbon grids (Quantifoil) glow-discharged 60 s using a PELCO glow-discharge system (Ted Pella); grids were blotted with #595 filter paper (Ted Pella) for 7-8 s at 22°C, flash-frozen by plunging in a liquid ethane cooled with liquid N$_2$, and stored in liquid N$_2$.

Cryo-EM structure determination: data collection and data reduction: λtR1-NusG-Rho-TEC (n = 6)

Cryo-EM data for λtR1-NusG-Rho-TEC (n = 6) were collected at the National Center for CryoEM Access and Training (NCCAT), using a 300 kV Krios Titan (FEI/ThermoFisher) electron microscope equipped with a Gatan K2 Summit direct electron detector (Gatan), Leginon software[43], a nominal magnification of 81,000x, a calibrated pixel size of 1.069 Å/pixel, and a dose rate of 35 electrons/Å^2/s. Movies were recorded at 30 ms/frame for 1.5 s (50 frames), resulting in a total radiation dose of 53 electrons/Å^2. Defocus range was varied from −1.25 to −2.5. A total of 15,559 micrographs were recorded from one grid over three days. Micrographs were gain-normalized and defect-corrected.

Data were processed as summarized in Extended data Fig. 3. Data processing was performed using a Tensor TS4 Linux GPU workstation with four GTX 1080 Ti graphic cards (NVIDIA). Dose weighting and motion correction (3x3 tiles; b-factor = 150) were performed using Motioncor2[44]. CTF estimation was performed using CTFFIND-4.1[45]. Subsequent image processing was performed using Relion 3.0[46]. Automatic particle picking with Laplacian-of-Gaussian filtering yielded an initial set of 6,257,721 particles. Particles were extracted into 512x512 pixel boxes and subjected to rounds of reference-free 2D classification and removal of poorly populated classes, yielding a selected set of 69,316 particles. The selected set was 3D-classified with C1 symmetry, using a 3D template created *ab initio* using 3D_initial_model under Relion 3.0. Classes that exhibited strong, well-defined density for both Rho and the TEC were selected, 36,044 particles for the selected classes were combined, were 3D auto-refined using a mask with diameter of 200 Å, and were subjected to masked multi-body refinement using the Rho and TEC masks, yielding a reconstruction with a global resolution that reached 4.3 Å, as determined from gold-standard Fourier shell correlation (Extended data Fig. 3d; Extended data Table 1; Supplementary Table 1). The reconstruction showed clear density for Rho, NusG, TEC, PBS-ligand RNA, SBS-ligand RNA, and spacer RNA (Extended data Fig. 3e–i).

The initial atomic model for λtR1-NusG-Rho-TEC (n = 6) was built by docking of (i) the Rho hexamer, one copy of NusG-C, and Mg-ADP-BeF$_3$ from a crystal structure of *E. coli* Rho hexamer interacting with six copies of *E. coli* NusG-C and Mg-ADP-BeF$_3$ (PDB 6DUQ)[23], (ii) SBS-ligand RNA from a crystal structure of a *E. coli* Rho hexamer interacting with SBS-ligand RNA and Mg-ADP-BeF$_3$ (PDB 5JJI)[22], and (iii) NusG-N, NusG linker, and the TEC from a cryo-EM structure of a complex of *E. coli* NusG bound to an *E. coli* TEC (PDB 6ZTJ)[34], using Chimera[47]. PBS-ligand RNA, spacer RNA, and the double-stranded DNA upstream of the TEC were built manually using Chimera and Coot[47–48]. For the Rho and C-termini (residues 418-420), the NusG N- and C-termini (residues 1-5 and 181-182), RNAP β' N- and C-termini and trigger loop (residues 1 and 934-947, 1127-1135, and 1374-1408), RNAP β N- and C-termini (residues 1 and 1342-1343), RNAP α^I and α^{II} N-termini, activation-target loops, and C-terminal domains (residues 1-4, 159-164, and 234-329), and RNAP ω N- and C-termini (residues 1-2 and 75-92), density was absent, suggesting high segmental flexibility; these segments were not fitted.

Rigid-body refinement of TEC and Rho against the map was performed using real_space_refine under Phenix[49]. PBS-ligand RNA, SBS-ligand RNA, spacer RNA, NusG-

N (residues 45-62), NusG-C (residues 130-180), the NusG linker (residues 104-129), RNAP β' ZBD (residues 62-95), RNAP β FTH (residues 890-912), and double-stranded DNA upstream of the TEC were subjected to iterative cycles of model building and refinement in Coot[48]. Structure visualization was performed using Pymol (Schrödinger).

The final density maps for λtR1-NusG-Rho-TEC (n = 6) were deposited in the EMDB with accession codes EMD-27930 (map, processed by focused refinement, for TEC, NusG, and spacer RNA), EMD-27928 (map, processed by focused refinement, for Rho, PBS-ligand RNA, SBS-ligand RNA, and Mg-ADP-BeF$_3$), and EMD-27929 (lower-resolution map of full complex, without focused refinement to improve resolution of components), and the final atomic coordinates were deposited in the PDB with accession codes PDB 8E6X (coordinates for TEC, NusG, SBS RNA, and spacer RNA) and PDB 8E6W (coordinates for Rho, PBS-ligand RNA, and Mg-ADP-BeF$_3$) (Table S1).

Cryo-EM structure determination: data collection and data reduction: dC75-NusG-Rho-TEC (n = 6)

Cryo-EM data for dC75-NusG-Rho-TEC (n = 6) were collected at NCCAT, using a 300 kV Krios Titan (FEI/ThermoFisher) electron microscope equipped with a Gatan K2 Summit direct electron detector (Gatan) and Leginon software[43], using procedures as in the preceding section. A total of 16,394 micrographs were recorded from one grid over three days. Micrographs were gain-normalized and defect-corrected.

Data were processed as summarized in Extended data Fig. 4, using procedures as in the preceding section. Data processing yielded a reconstruction at 4.7 Å resolution (Extended data Fig. 4d; Extended data Table 1; Supplementary Table 1). Atomic models were built and refined as in the preceding section.

The final density maps of dC75-NusG-Rho-TEC (n = 6) were deposited in the EMDB with accession codes EMD-27931 (map, processed by focused refinement, for TEC, NusG, and spacer RNA), EMD-27932 (map, processed by focused refinement, for Rho, PBS-ligand RNA, SBS-ligand RNA, and Mg-ADP-BeF$_3$), and EMD-27933 (lower-resolution map of full complex, without focused refinement to improve resolution of components), and the final atomic coordinates were deposited in the PDB with accession codes PDB 8E6Z (coordinates for TEC, NusG, SBS RNA, and spacer RNA) and PDB 8E70 (coordinates for Rho, PBS-ligand RNA, and Mg-ADP-BeF$_3$) (Table S1).

Cryo-EM structure determination: data collection and data reduction: NusG-Rho-TEC (n = 6. 7, and 8)

Cryo-EM data for NusG-Rho-TEC (n = 6) and NusG-Rho-TEC (n = 7) were collected at the Rutgers CryoEM and Nanoimaging Facility, using a 200 kV Talos Arctica (FEI/ThermoFisher) electron microscope equipped with a K2 Summit and Bioquantum energy filter (Gatan), SerialEM software[50], a nominal magnification of 130,000x, a calibrated pixel size of 1.038 Å/pixel, and a dose rate of 5 electrons/pixel/s , movies at 200 ms/frame for 6 s (30 frames; total radiation dose of 28 electrons/Å^2), and a defocus range of −1.25 μm to −2.5 μm. A total of 2,784 micrographs were recorded for NusG-Rho-TEC (n = 6) from one

grid over one day, and a total of 8,528 micrographs were recorded for NusG-Rho-TEC (n = 7) from one grid over two days. Micrographs were gain-normalized and defect-corrected.

Cryo-EM data for NusG-Rho-TEC (n = 8) were collected at the Stanford-SLAC Cryo-EM Center (SLAC), using a 300 kV Krios Titan (FEI/ThermoFisher) electron microscope equipped with a Gatan K2 Summit direct electron detector (Gatan), SerialEM software, a nominal magnification of 81,000x, a calibrated pixel size of 1.0 Å/pixel, a dose rate of 55 electrons/Å^2/s, movies at 35 ms/frame for 1.1 s (30 frames;, total radiation dose of 50 electrons/Å^2), and a defocus range of −1.25 μm to −2.5 μm. A total of 15,340 microphotographs were recorded from one grid over three days. Micrographs were gain-normalized and defect-corrected.

Data were processed as summarized in Extended data Fig. 5, using procedures as in the preceding two sections. Data processing yielded reconstructions at 6.5, 4.4, and 4.2 Å resolution for NusG-Rho-TEC (n = 6), NusG-Rho-TEC (n = 7) , and NusG-Rho-TEC (n = 8) , respectively (Extended data Fig. 5d; Extended data Table 1; Supplementary Table 1). Atomic models were built and refined as in the preceding two sections.

The final density maps of NusG-Rho-TEC (n = 6) were deposited in the EMDB with accession codes EMD-27864 (map, processed by focused refinement, for TEC, NusG, and spacer RNA), EMD-27865 (map, processed by focused refinement, for Rho, PBS-ligand RNA, SBS-ligand RNA, and Mg-ADP-BeF$_3$), and EMD-27897 (lower-resolution map of full complex, without focused refinement to improve resolution of components), and the final atomic coordinates were deposited in the PDB with accession codes PDB 8E3F (coordinates for TEC, NusG, SBS RNA, and spacer RNA) and PDB 8E3H (coordinates for Rho, PBS-ligand RNA, and Mg-ADP-BeF$_3$) (Table S1).

The final density maps of NusG-Rho-TEC (n = 7) were deposited in the EMDB with accession codes EMD-27913 (map, processed by focused refinement, for TEC, NusG, and spacer RNA), EMD-27914 (map, processed by focused refinement, for Rho, PBS-ligand RNA, SBS-ligand RNA, and Mg-ADP-BeF$_3$), and EMD-27915 (lower-resolution map of full complex, without focused refinement to improve resolution of components), and the final atomic coordinates were deposited in the PDB with accession codes PDB 8E5K (coordinates for TEC, NusG, SBS RNA, and spacer RNA) and PDB 8E5L (coordinates for Rho, PBS-ligand RNA, and Mg-ADP-BeF$_3$) (Table S1).

The final density maps of NusG-Rho-TEC (n = 8) were deposited in the EMDB with accession codes EMD-27916 (map, processed by focused refinement, for TEC, NusG, and spacer RNA), EMD-27917 (map, processed by focused refinement, for Rho, PBS-ligand RNA, SBS-ligand RNA, and Mg-ADP-BeF$_3$), and EMD-27918 (lower-resolution map of full complex, without focused refinement to improve resolution of components), and the final atomic coordinates were deposited in the PDB with accession codes PDB 8E5O (coordinates for TEC, NusG, SBS RNA, and spacer RNA) and PDB 8E5P (coordinates for Rho, PBS-ligand RNA, and Mg-ADP-BeF$_3$) (Table S1).

Extended Data

Extended data Fig. 1. Scaffold assay for Rho-dependent termination: additional data
(a) Top, synthetic nucleic-acid scaffolds containing complementary nontemplate and template DNA strands (colors as in Fig. 1b). Bottom, RNA-release data assessing Rho-dependent termination in complexes containing NusG (left), NusG-N (center), or no NusG (right). Asterisks, released RNA products that exhibit increased levels relative to control reactions lacking Rho (lanes 6 and 7 of each subpanel). Termination is detected by an

increase in released RNA products relative to control reactions lacking Rho. Assays were performed twice with consistent results.

(b) As in (a), except that synthetic nucleic-acid scaffolds contain noncomplementary nontemplate and template DNA strands.

The PBS ligands λtR1 *rut* and dC75 support efficient termination under these conditions (lanes 1 and 2 of each gel panel), but the shorter PBS ligands dC5 and dC15 do not (lanes 3 and 4 of each gel subpanel). It has been shown previously that dC15 and dC5 exhibit lower binding affinities for Rho than dC75, exhibiting half-maximally saturating concentrations 30-fold and 150-fold, respectively, the half-maximally saturating concentrations for dC75.[21] The PBS ligand λtR1 *rut* supports efficient and immediate termination under these conditions; with λtR1 *rut*, ~100 % of RNA is released before RNA extension (lane 1 of each gel panel). The PBS ligand dC75 supports efficient but less immediate termination under these conditions; with dC75, in the experiments of (b), ~100 % of RNA is released before RNA extension (lane 1 of each gel panel), but, in the experiments of (a), ~30% of RNA is released before RNA extension, and ~70% of RNA is released only after RNA extension by 1 nt or 2 nt (lane 2 of each gel panel). The results indicate that both λtR1 *rut* and dC75 are effective PBS ligands and that λtR1 *rut* is a more effective PBS ligand than dC75 (see Extended data Fig. 2).

Extended data Fig. 2. Scaffold assay for Rho-dependent termination: additional data
(a) Top, synthetic nucleic-acid scaffolds containing complementary nontemplate and
template DNA strands (colors as in Fig. 1b; Extended data Fig. 1). Bottom, RNA-extension
data assessing Rho-dependent termination in complexes having λtR1 *rut* as PBS ligand
(odd-numbered lanes) or dC75 as PBS ligand (even-numbered lanes) on scaffolds where the
U-rich-RNA-segment length, n, is 4, 5, 6, 7, 8 or 9 codons (first, second, third, fourth, fifth,
and sixth subpanels). Red asterisks, RNA products that exhibit increased levels compared to
control reactions without PBS ligand; open circles, RNA products that exhibit decreased
levels relative to control reactions without PBS ligand. Termination is detected by an
increase in unextended and partly extended RNA products (lower and central bands), and
a decrease in fully extended RNA products (top bands). Assays were performed twice with
consistent results.

(b) As in (a), except that **s**ynthetic nucleic-acid scaffolds contain noncomplementary nontemplate and template DNA strands.

The PBS ligand λtR1 rut supports efficient and immediate termination under these conditions; with λtR1 rut, ~100% of RNA synthesis ceases before RNA extension (lane 1 of each gel panel). The PBS ligand dC75 supports efficient but less immediate termination under these conditions; with dC75, ~30% of RNA synthesis ceases before RNA extension, and ~70% of RNA synthesis ceases only after RNA extension by 1 nt or 2 nt (lane 2 of each gel panel). The results indicate that both λtR1 rut and dC75 are effective PBS ligands and that λtR1 *rut* is a more effective PBS ligand than dC75 (see Extended data Fig. 1).

All six tested U-rich-RNA-segment lengths (n = 4, 5, 6, 7, 8, and 9 codons) support termination. In the experiments of (a), the six tested U-rich-RNA-segment lengths support termination comparably efficiently. In the experiments of (b), shorter lengths (n = 4, 5, and 6 codons) support termination more efficiently than longer lengths (n = 7, 8, and 9 codons).
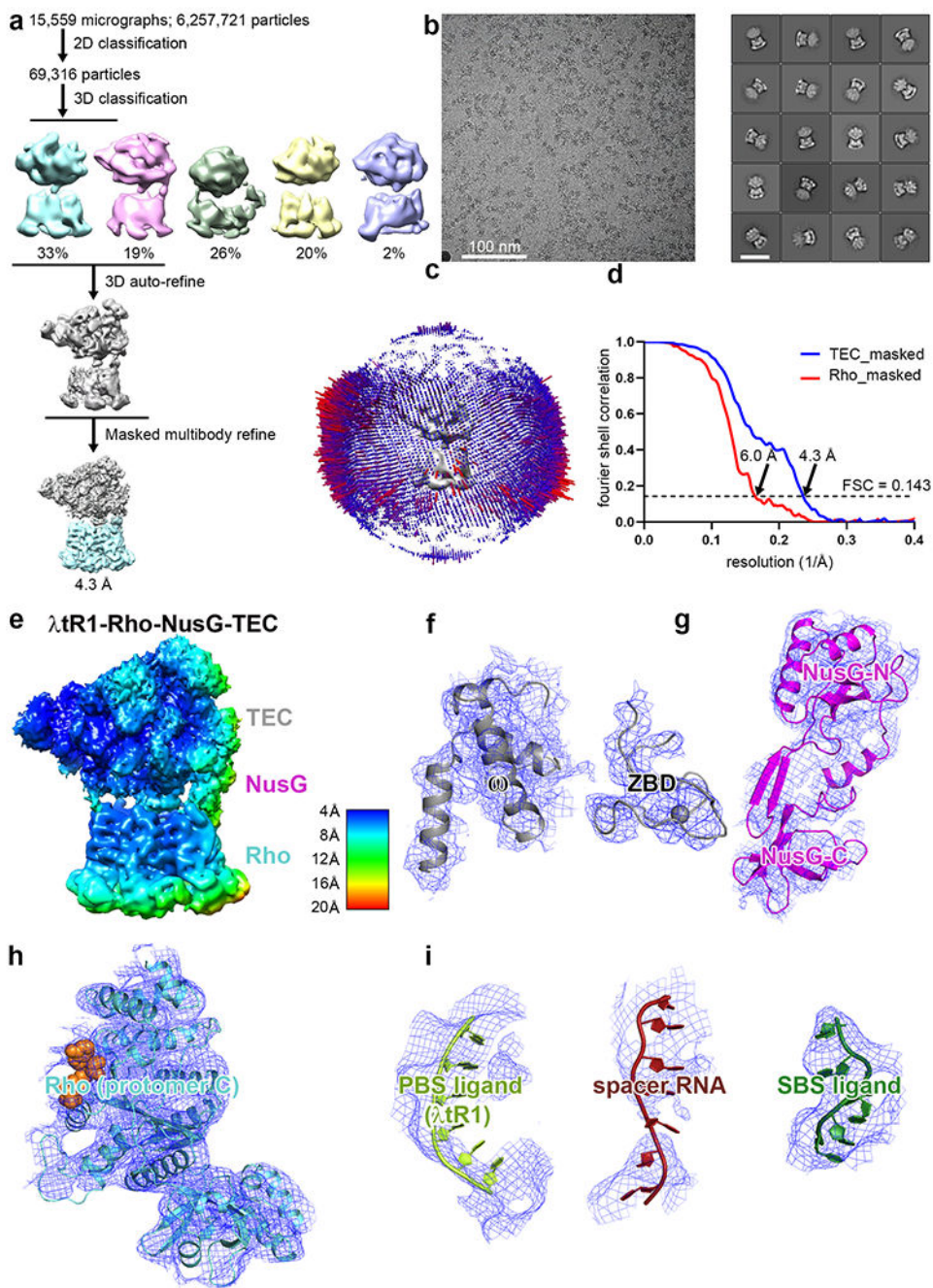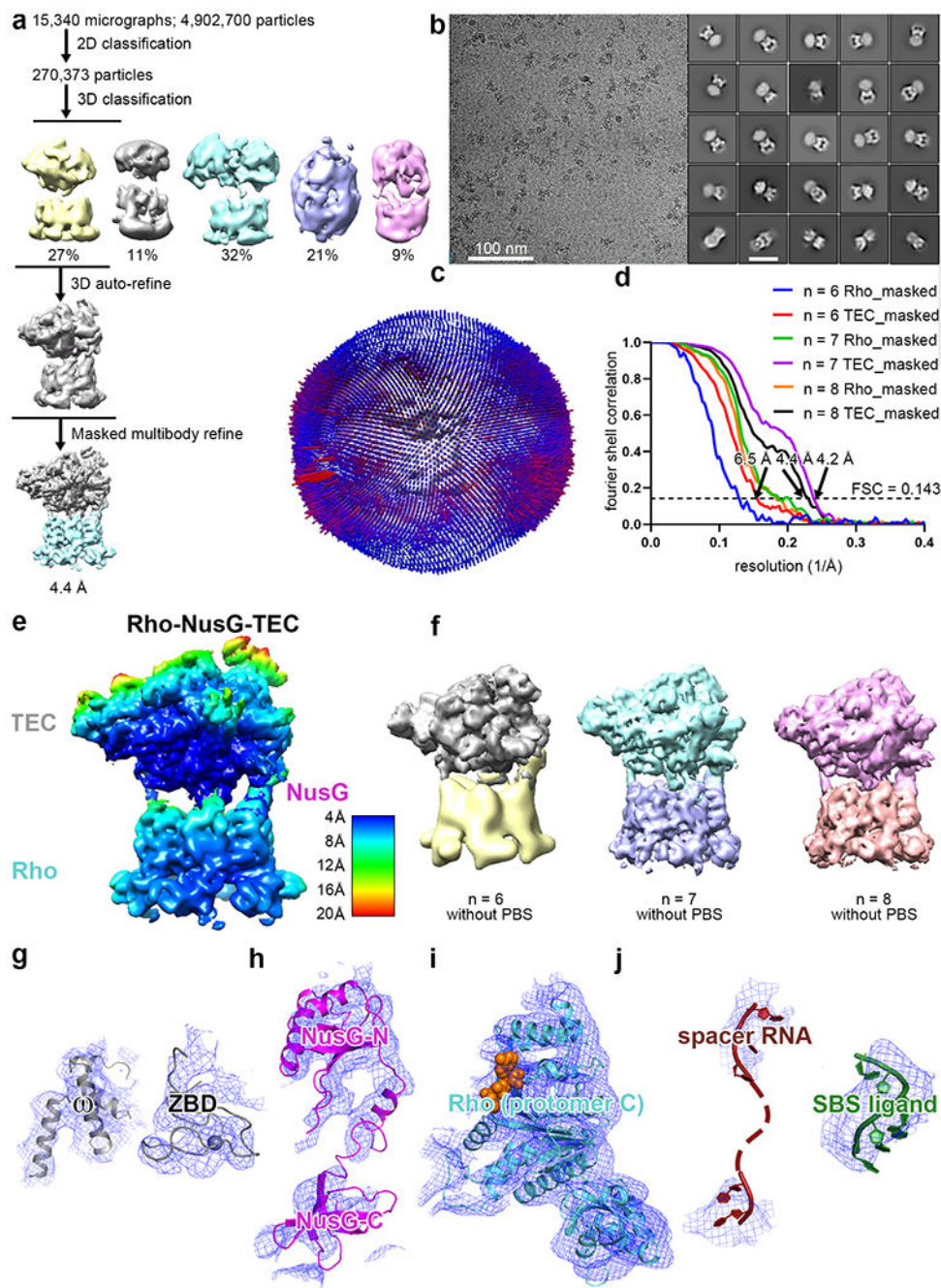
Extended data Fig. 3. Structure determination: λtR1-NusG-Rho-TEC (n = 6)

**(a)** Data processing scheme (Table S1).

(b) Representative electron microphotograph and 2D class averages (50 nm scale bar in right subpanel).

(c) Orientation distribution.

(d) Fourier-shell correlation (FSC) plot.

(e) EM density map colored by local resolution (view orientation as in Fig. 2a, left).

(f-i) Representative EM density (blue mesh) and fits (ribbons) for RNAP regions that interact with Rho, NusG, Rho protomer C, PBS ligand interacting with Rho protomer C, spacer RNA, and SBS ligand.
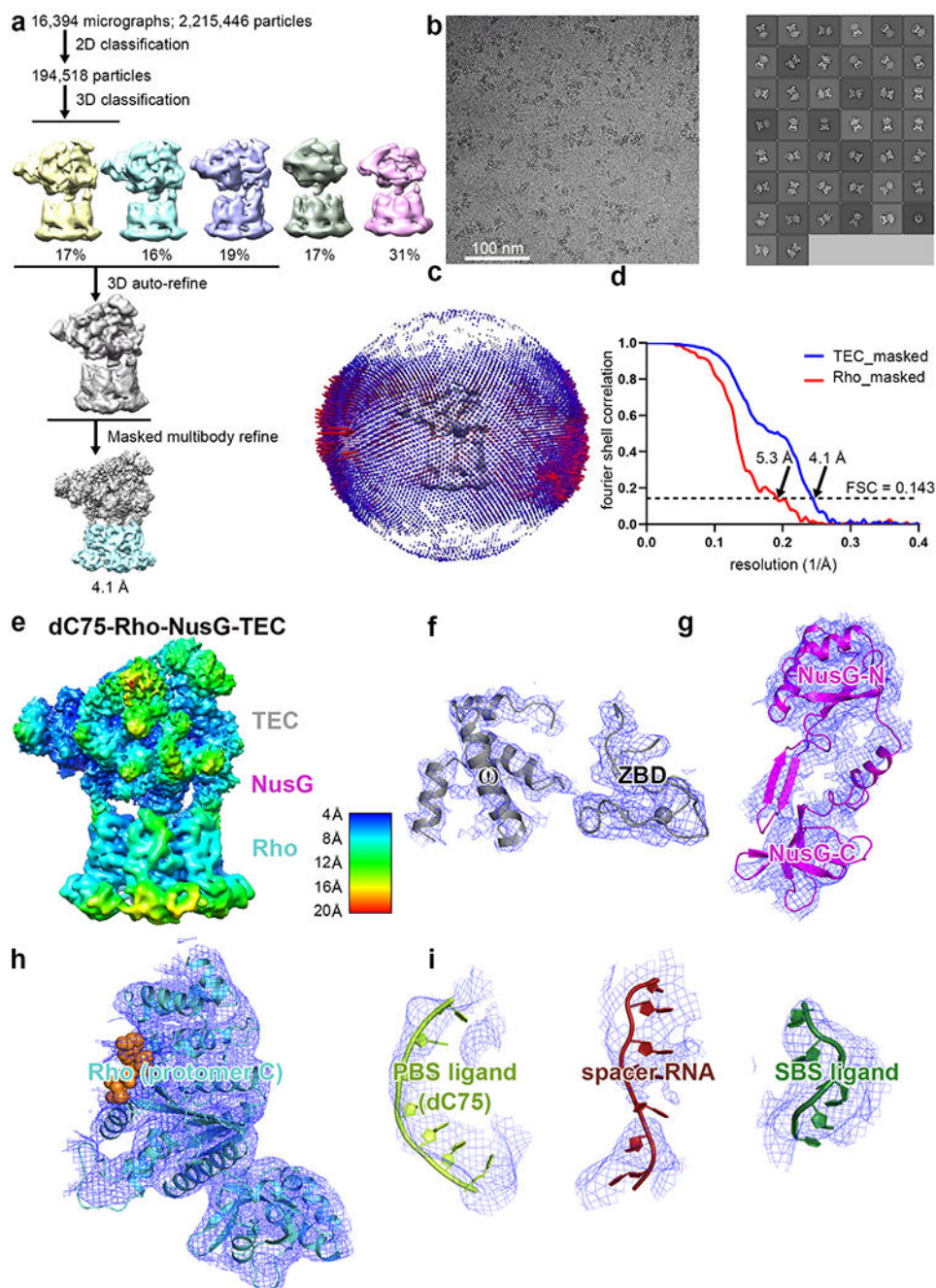

Extended data Fig. 4. Structure determination: dC75-NusG-Rho-TEC (n = 6)
(a) Data processing scheme (Table S1).
(b) Representative electron microphotograph and 2D class averages (50 nm scale bar in right subpanel).

(c) Orientation distribution.

(d) Fourier-shell correlation (FSC) plot.

(e) EM density map colored by local resolution (view orientation as in Fig. 2a, left).

(f-i) Representative EM density (blue mesh) and fits (ribbons) for RNAP regions that interact with Rho, NusG, Rho protomer C, PBS ligand interacting with Rho protomer C, spacer RNA, and SBS ligand.

Extended data Fig. 5. Structure determination: NusG-Rho-TEC (n = 6, 7, and 8)

(a) Data processing scheme (n = 8).

(b) Representative electron microphotograph and 2D class averages (n = 8; 50 nm scale bar in right subpanel).

(c) Orientation distribution (n = 8).

(d) Fourier-shell correlation (FSC) plot.

(e) EM density map colored by local resolution (n = 8) (view orientation as in Fig. 2a, left).

(f) EM density maps for NusG-Rho-TEC obtained using nucleic acid scaffolds with n = 6, 7, and 8 (view orientation as in Fig. 2a, left).

(g-j) Representative EM density (blue mesh) and fits (ribbons) for RNAP regions that interact with Rho, NusG, Rho protomer C, spacer RNA, and SBS ligand.
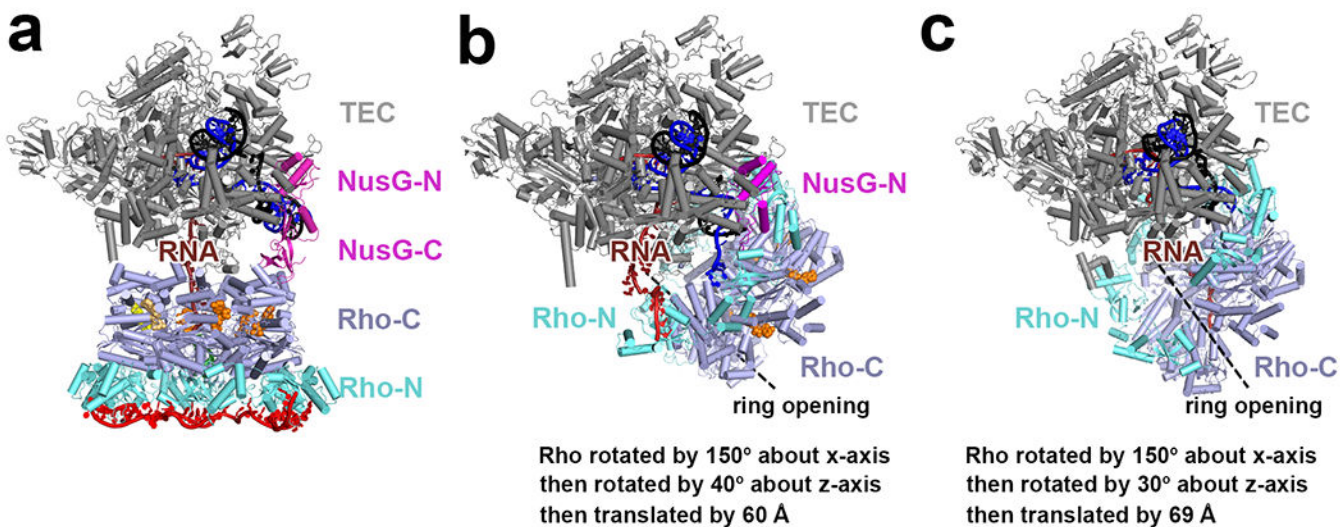
Extended data Fig. 6. Comparison of structure of λtR1-NusG-Rho-TEC to structures of Rho-TEC complexes of *30* and *31*

(a) Structure of λtR1-NusG-Rho-TEC. Rho N-terminal domain (Rho-N); cyan, and Rho C-terminal domain (Rho-C), slate blue, are shown in different colors to highlight orientation of Rho domains relative to the TEC. View orientation and other colors as in Fig. 2a, left.

(b)-(c) Structures of Rho-TEC complexes of *30* (B; PDB 6Z9R) and *31* (C; PDB 6XAS; NusA omitted for clarity). View orientation that superimposes TEC atoms in (b) and (c) on TEC atoms in (a). Colors as in (a). The ring opening of the open-ring Rho hexamer in structures of *30* and *31* is indicated by a dashed line, and rotations and translation that relate the orientation of Rho relative to the TEC in structures of *30* and *31* to those in (a) are summarized below.
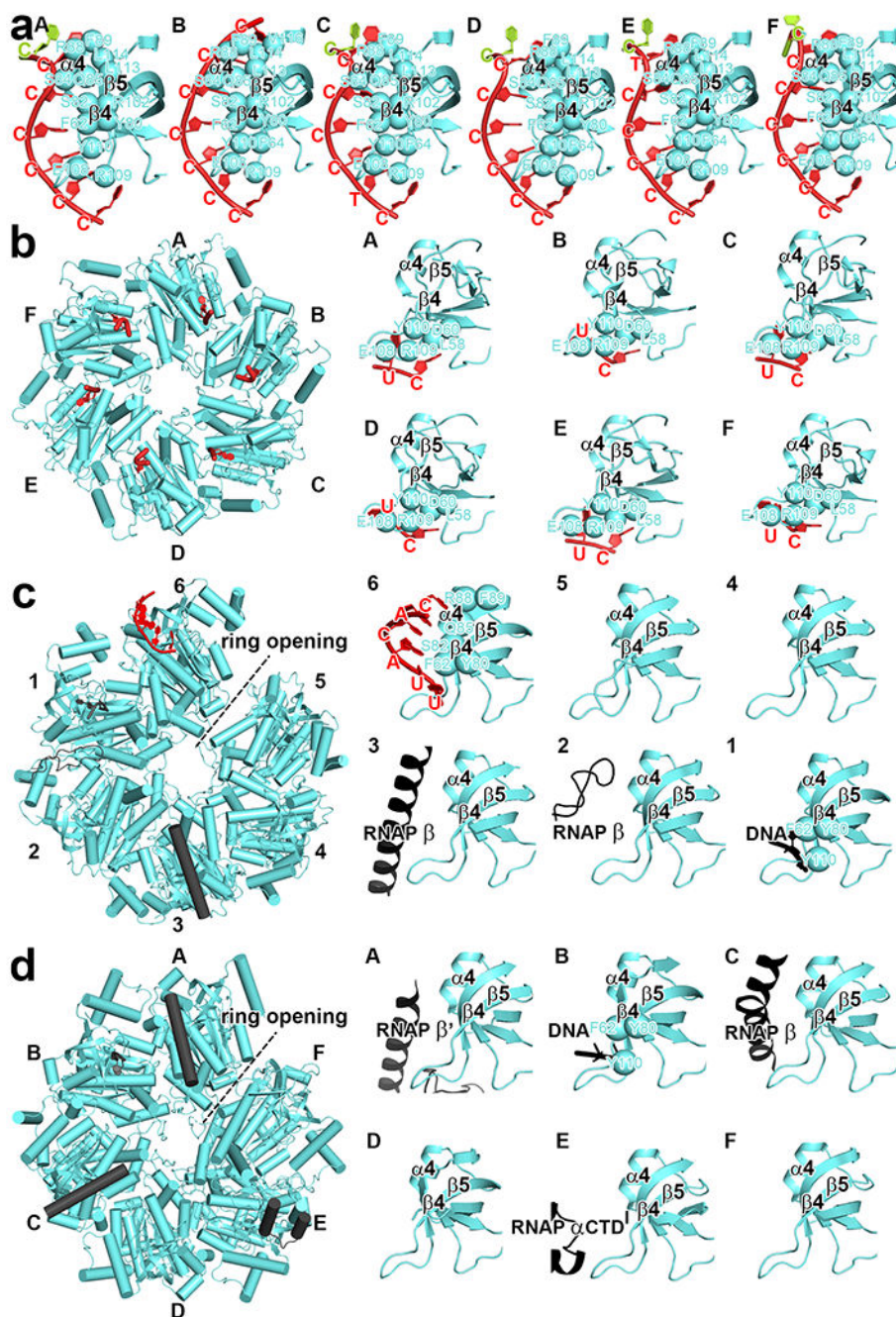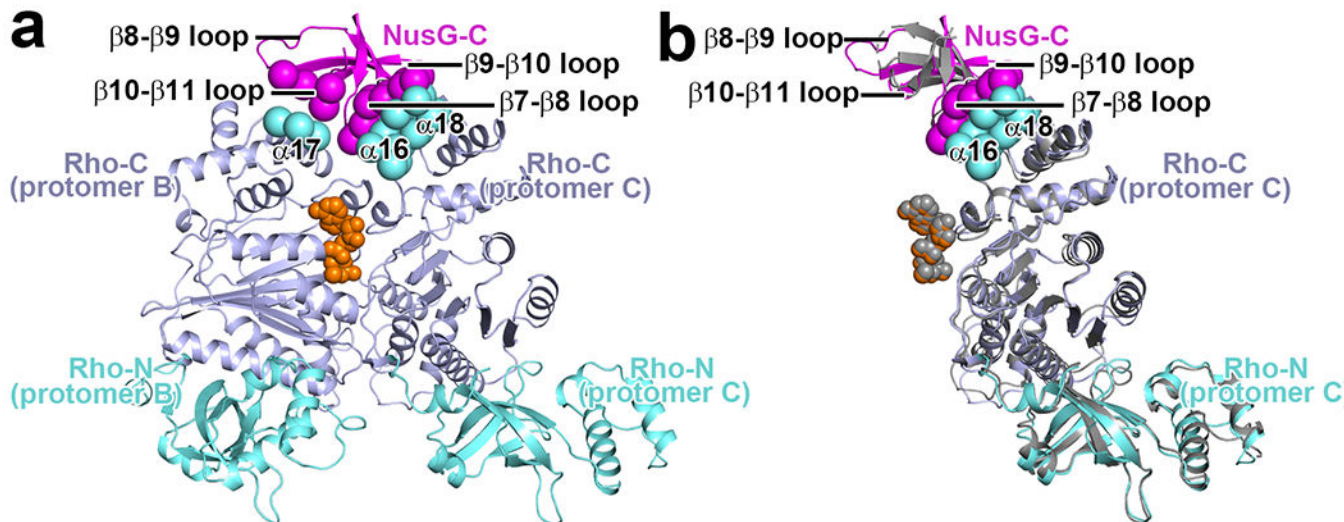
Extended data Fig. 7. Protein-RNA interactions between PBS ligand and Rho PBS

(a) Rho-(PBS ligand) interactions in dC75-NusG-Rho-TEC. View orientations and colors as in Fig. 3a, top right.

(b) Rho-(PBS ligand) interactions in crystal structure of Rho hexamer interacting with six copies of oligoribonucleotide in absence of NusG and TEC (PDB 2HT1)[17]. View orientations and colors as in Fig. 3a, top. Oligoribonucleotides non-specifically interacting with Rho-C omitted for clarity.

(c)-(d) Rho-(PBS ligand) interactions in structures of *30* (panel c; PDB 6Z9R) and *31* (panel d; PDB 6XAS). Dashed black lines, ring openings in open-ring Rho hexamers in structures of *30* and *31*; black cylinders and black ribbons, RNAP or DNA structural elements of that occlude PBS-binding sites, preventing interaction with PBS ligand in structures of *30* and *31*. View orientations and other colors as in Fig. 3a, top.


Extended data Fig. 8. Protein-protein interactions between NusG-C and Rho

(a) Rho-(NusG-C) interactions in λtR1-NusG-Rho-TEC. Colors as in Extended data Fig. 6.
(b) Superimposition of NusG-C and Rho protomer C of λtR1-NusG-Rho-TEC [colored as in (a)] on structure of one NusG-C and one Rho protomer in crystal structure of Rho hexamer interacting with six copies of a NusG-C protein fragment in absence of TEC (PDB 6DUQ; gray)[23]. Dashed grey ribbon, disordered segment of NusG-C β8-β9 loop in crystal structure.

The interaction between NusG-C and Rho protomer B [see (a)] is not present in the crystal structure of Rho hexamer interacting with six copies of NusG-C protein fragment[23] [see (b)], apparently because steric clash between adjacent NusG-C protein fragments in that structure resulted in disorder of the NusG β8-β9 loop and disruption of interactions made by the NusG β8-β9 and β10-β11 loops [dashed lines in (b)].
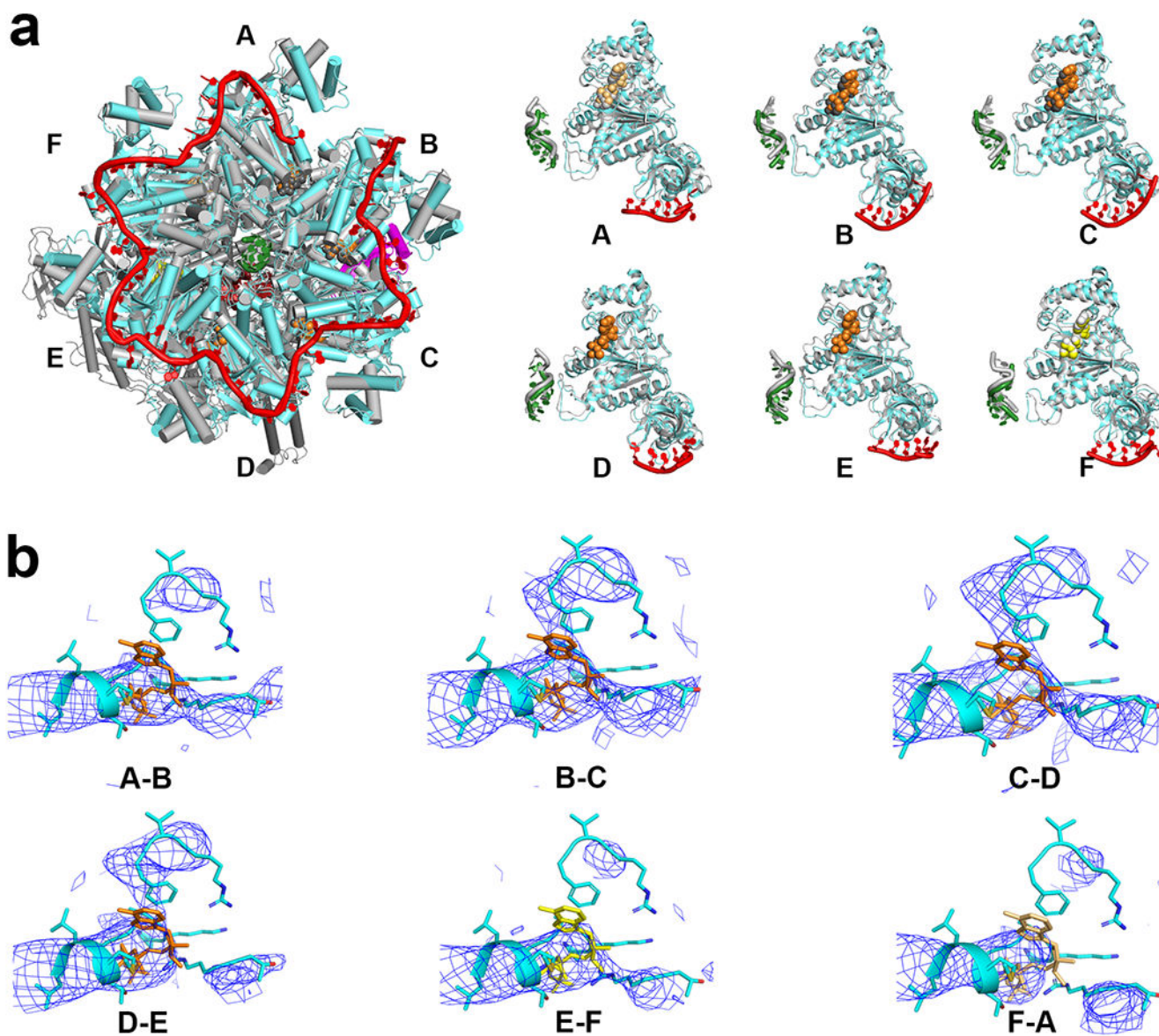
Extended data Fig. 9. Motor states of Rho hexamer

(a) Left, superimposition of structure of λtR1-NusG-Rho-TEC (colored as in Fig. 2a, left) on crystal structure of Rho hexamer interacting with SBS ligand and Mg-ADP-BeF₃ in absence of NusG and TEC (PDB 5JJI; colored gray)[22]. View orientation as in Fig. 2a, left. TEC omitted for clarity. Right, **s**uperimposition of Rho protomers A-F interacting with PBS ligand, SBS ligand, and Mg-ADP-BeF₃ in structure of λtR1-NusG-Rho-TEC [colored as in (a)] on crystal structure of Rho protomers A-F interacting with SBS ligand and Mg-ADP-BeF₃ (PDB 5JJI; gray)[22].

(b) Occupancy and order of ATP-binding sites of λtR1-NusG-Rho-TEC. Figure presents EM density (blue mesh) and fit (cyan for Rho; orange, light orange, and yellow for Mg-ADP-BeF₃ at high, low, and very low occupancies, respectively) for ATP binding sites between Rho protomers A and B, B and C, C and D, D and E, E and F, and F and A.
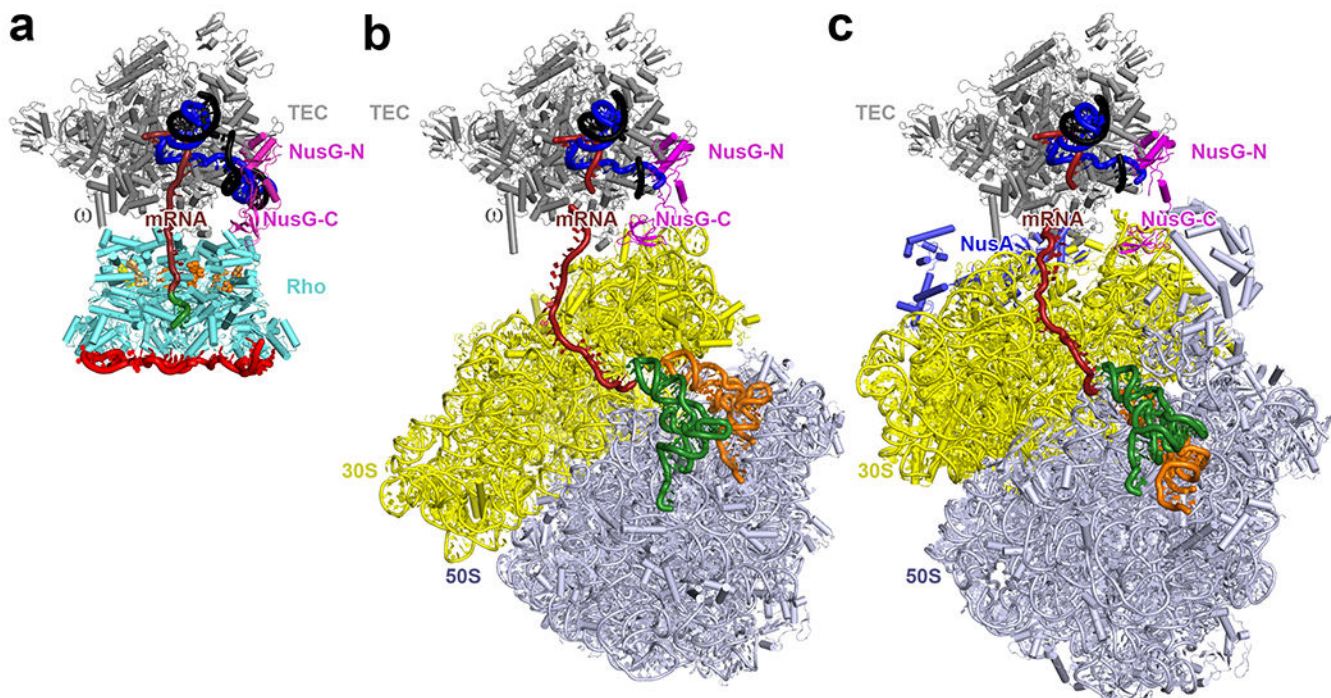
Extended data Fig. 10. Comparison of structure of λtR1-NusG-Rho-TEC to structures of functional transcription-translation complexes NusG-TTC-B and NusA-NusG-TTC-B
(a) Structure of λtR1-NusG-Rho-TEC. View orientation and colors as in Fig. 2a, left.
(b)-(c) Structures of NusG-TTC-B (B; PDB 6XII)[34–35] and NusA-NusG-TTC-B (C; PDB 6X7F)[35]. View orientation that superimposes TEC atoms in (B) and (C) on TEC atoms in (A). Ribosome 30S subunit, yellow; ribosome 50S subunit, gray; P- and E-site tRNAs bound to ribosome, green and orange; NusA, light blue. Other colors as in (a).

Extended data Table 1:

Cryo-EM data collection, refinement, and validation statistics

	λtR1-Rho-NusG-TEC (EMDB 27928, 27929, 27930) (PDB 8E6X, 8E6W)	dC75-Rho-NusG-TEC (EMDB 27931, 27932, 27933) (PDB 8E6Z, 8E70)
Data collection and processing		
Magnification	81,000x	81,000x
Voltage (kV)	300	300
Electron exposure (e–/Å²)	53	53
Defocus range (μm)	–1.25 to –2.5	–1.25 to –2.5
Pixel size (Å)	1.069	1.069
Symmetry imposed	C1	C1
Initial particle images (no.)	15,559	16,394
Final particle images (no.)	14,431	12,275
Map resolution (Å)	4.3	4.1
FSC threshold	0.143	0.143
Map resolution range (Å)	4.3-6.0	4.1-5.3

	λtR1-Rho-NusG-TEC (EMDB 27928, 27929, 27930) (PDB 8E6X, 8E6W)	dC75-Rho-NusG-TEC (EMDB 27931, 27932, 27933) (PDB 8E6Z, 8E70)
Refinement		
Initial model used (PDB code)	6DUQ, 5JJI, 6ZTJ	6DUQ, 5JJI, 6ZTJ
Model resolution (Å)	4.3	4.1
FSC threshold		

	Rho-NusG-TEC (n=6) (EMDB 27864, 27865, 27897) (PDB 8E3F, 8E3H)	Rho-NusG-TEC (n=7) (EMDB 27913, 27914, 27915) (PDB 8E5K, 8E5L)	Rho-NusG-TEC (n = 8) (EMDB 27916, 27917, 27918) (PDB 8E5O, 8E5P)
Data collection and processing			
Magnification	130,000x	130,000x	81.000x
Voltage (kV)	200	200	300
Electron exposure (e–/Å^2)	28	28	50
Defocus range (μm)	−1.25 to −2.5	−1.25 to −2.5	−1.25 to −2.5
Pixel size (Å)	1.039	1.039	1.1
Symmetry imposed	C1	C1	C1
Initial particle images (no.)	2,784	8,528	15,340
Final particle images (no.)	2,546	7,422	14,323
Map resolution (Å)	6.5	4.2	4.4
FSC threshold	0.143	0.143	0.143
Map resolution range (Å)	6.5-14.2	4.2-6.0	4.4-7.4
Refinement			
Initial model used (PDB code)	6DUQ, 5JJI, 6ZTJ	6DUQ, 5JJI, 6ZTJ	6DUQ, 5JJI, 6ZTJ
Model resolution (Å)	6.5	4.2	4.4
FSC threshold			

Supplementary Material

Refer to Web version on PubMed Central for supplementary material.

Acknowledgments

Data availability statement

Cryo-EM maps have been deposited in the Electron Microscopy Database (EMDB accession codes EMD-27928, EMD-27929, EMD-27930, EMD-27931, EMD-27932, EMD-27933, EMD-27864, EMD-27865, EMD-27897, EMD-27913, EMD-27914, EMD-27915, EMD-27916, EMD-27917, and EMD-27918), and atomic coordinates have been deposited in the Protein Database (PDB accession codes 8E3F, 8E3H, 8E5K, 8E5L, 8E5O, 8E5P, 8E6W, 8E6X, 8E6Z, and 8E70). Unique biological materials will be made available to qualified investigators on request.

References

1. Ray-Soni A, Bellecourt M & Landick R Mechanisms of bacterial transcription termination. Annu. Rev. Biochem 85, 319–347 (2016). [PubMed: 27023849]

2. Mitra P, Ghosh G, Hafeezunnisa M & Sen R Rho protein: roles and mechanisms. Annu. Rev. Microbiol 71, 687–709 (2017). [PubMed: 28731845]

3. Roberts J Mechanisms of bacterial transcription termination. J. Mol. Biol 431, 4030–4039 (2019). [PubMed: 30978344]

4. Sunday N, Svetlov D & Artsimovitch I Rho termination factor: one ring to bind them all. In RNA Polymerases as Molecular Motors, Second Edition, eds. Landick R, Wang J & Strick T (Cambridge, United Kingdom, RSC Publishing), pp. 100–131 (2021).

5. Roberts J Termination factor for RNA synthesis. Nature 224, 1168–1174 (1969). [PubMed: 4902144]

6. Bektesh S & Richardson J A Rho-recognition site on phage lambda cro-gene mRNA. Nature 283, 102–104 (1980). [PubMed: 6444243]

7. Brennan C, Dombroski A & Platt T Transcription termination factor Rho is an RNA-DNA helicase. Cell 48, 945–952 (1987). [PubMed: 3030561]

8. Dombroski AJ & Platt T Structure of Rho factor: an RNA-binding domain and a separate region with strong similarity to proven ATP-binding domains. Proc. Natl. Acad. Sci. USA 85, 2538–2542 (1988). [PubMed: 2451828]

9. Alifano P, Rivellini F, Limauro D, Bruni C & Carlomagno M A consensus motif common to all Rho-dependent prokaryotic transcription terminators. Cell 64, 553–563 (1991). [PubMed: 1703923]

10. Jin DJ, Burgess R, Richardson J & Gross C Termination efficiency at rho-dependent terminators depends on kinetic coupling between RNA polymerase and Rho. Proc. Natl. Acad. Sci. USA 89, 1453–1457 (1992). [PubMed: 1741399]

11. Sullivan SL & Gottesman ME Requirement for E. coli NusG protein in factor-dependent transcription termination. Cell 68, 989–994 (1992). [PubMed: 1547498]

12. Seifried S, Easton J & von Hippel P ATPase activity of transcription-termination factor rho. Proc. Natl. Acad. Sci. USA 89, 10454–10458 (1992). [PubMed: 1438233]

13. Geiselmann J, Wang Y, Seifried S & von Hippel P A physical model for the translocation and helicase activities of Escherichia coli transcription termination protein Rho. Proc. Natl. Acad. Sci. USA 90, 7754–7758 (1993). [PubMed: 7689228]

14. Steinmetz E & Platt T Evidence supporting a tethered tracking model for helicase activity of *Escherichia coli* Rho factor. Proc. Natl. Acad. Sci. USA 91, 1401–1405 (1993).

15. Bogden C, Fass D, Bergman N, Nichols M & Berger J The structural basis for terminator recognition by the Rho transcription termination factor. Mol. Cell 3, 487–493 (1999). [PubMed: 10230401]

16. Skordalakes E & Berger J Structure of the Rho transcription terminator: mechanism of mRNA recognition and helicase loading. Cell 114, 135–146 (2003). [PubMed: 12859904]

17. Skordalakes E & Berger J Structural insights into RNA-dependent ring closure and ATPase activation by the Rho termination factor. Cell 127, 553–564 (2006). [PubMed: 17081977]

18. Park J & Roberts J Role of DNA bubble rewinding in enzymatic transcription termination. Proc. Natl. Acad. Sci. USA 103, 4870–4875 (2006). [PubMed: 16551743]

19. Epshtein V, Dutta D, Wade J & Nudler E An allosteric mechanism of Rho-dependent transcription termination. Nature 463, 245–249 (2010). [PubMed: 20075920]

20. Koslover D, Fazal F, Mooney R, Landick R & Block S Binding and translocation of termination factor rho studied at the single-molecule level. J. Mol. Biol 423, 664–676 (2012). [PubMed: 22885804]

21. Lawson MR, Dyer K & Berger JM Ligand-induced and small-molecule control of substrate loading in a hexameric helicase. Proc. Natl. Acad. Sci. USA 113, 13714–13719 (2016). [PubMed: 27821776]

22. Thomsen N, Lawson M, Witkowsky L, Qu S & Berger J Molecular mechanisms of substrate-controlled ring dynamics and substepping in a nucleic acid-dependent hexameric motor. Proc. Natl. Acad. Sci. USA 113, e7691–e7700 (2016). [PubMed: 27856760]

23. Lawson M, Ma W, Bellecourt M, Artsimovitch I, Martin A, Landick R, Schulten K & Berger J Mechanism for the regulated control of bacterial transcription termination by a universal adaptor protein. Mol, Cell 71, 911–922 (2018). [PubMed: 30122535]

24. Adhya S & Gottesman M Control of transcription termination. Annu. Rev. Biochem 47, 967–996 (1978). [PubMed: 354508]

25. Richardson JP Preventing the synthesis of unused transcripts by Rho factor. Cell 64, 1047–1049 (1991). [PubMed: 2004415]

26. Burmann B, Schweimer K, Luo X, Wahl M, Stitt B, Gottesman M & Rösch P A NusE:NusG complex links transcription and translation. Science 328, 501–504 (2010). [PubMed: 20413501]

27. Saxena S, Myka K, Washburn R, Costantino N, Court L & Gottesman E *Escherichia coli* transcription factor NusG binds to 70S ribosomes. Mol. Microbiol 108, 495–504 (2018). [PubMed: 29575154]

28. Washburn R, Zuber P, Sun M, Hashem Y, Shen B, Li W, Harvey S, Acosta Reyes F, Gottesman M, Knauer S & Frank J *Escherichia coli* NusG links the lead ribosome with the transcription elongation complex. iScience 23, 101352 (2020). [PubMed: 32726726]

29. Webster M & Weixlbaumer A Macromolecular assemblies supporting transcription-translation coupling. Transcription 12, 103–125 (2021). [PubMed: 34570660]

30. Said N, Hilal T, Sunday N, Khatri A, Burger J, Mielke T, Belogurov G, Loll B, Sen R, Artsimovitch I & Wahl M Steps toward translocation-independent RNA polymerase inactivation by terminator ATPase Rho. Science 371, eabd1673 (2021). [PubMed: 33243850]

31. Hao Z, Epshtein V, Kim KH, Proshkin S, Svetlov V, Kamarthapu V, Bharati B, Mironov A, Walz T & Nudler E Pre-termination transcription complex: structure and function. Mol. Cell 81, 281–292 (2021). [PubMed: 33296676]

32. Hao Z, Svetlov V & Nudler E Rho-dependent transcription termination: a revisionist view. Transcription 12, 171–181 (2021). [PubMed: 34705601]

33. Vassylyev D, Vassylyeva M, Perederina A, Tahirov T & Artsimovitch I Structural basis for transcription elongation by bacterial RNA polymerase. Nature 448, 157–162 (2007). [PubMed: 17581590]

34. Webster M, Takacs M, Zhu C, Vidmar V, Eduljee A, Abdelkareem M & Weixlbaumer A Structural basis of transcription-translation coupling and collision in bacteria. Science 369, 1355–1359 (2020). [PubMed: 32820062]

35. Wang C, Molodtsov V, Firlar E, Kaelber J, Blaha G, Su M & Ebright RH Structural basis of transcription-translation coupling. Science 369, 1359–1365 (2020). [PubMed: 32820061]

36. Kang J, Mooney R, Nedialkov Y, Saba J, Mishanina T, Artsimovitch I, Landick R & Darst S Structural basis for transcript elongation control by NusG family universal regulators. Cell 173, 1650–1662 (2018). [PubMed: 29887376]

37. Boyer P The ATP synthase--a splendid molecular machine. Annu. Rev. Biochem 66, 717–749 (1997). [PubMed: 9242922]

38. Guo X, Myasnikov G, Chen J, Crucifix C, Papai G, Takacs M, Schultz P & Weixlbaumer A Structural basis for NusA stabilized transcriptional pausing. Mol. Cell 69, 816–827 (2018). [PubMed: 29499136]

39. Murayama Y, Ehara H, Aoki M, Goto M, Yokoyama T, & Sekine S-I Structural basis of the transcription termination factor Rho engagement with transcribing RNA polymerase. bioRxiv. 10.1101/2022.09.02.506315 (2022).

Additional references associated with methods

40. Belogurov G, Vassylyeva M, Svetlov V, Klyuyev S, Grishin N, Vassylyev D, and Artsimovitch I Structural basis for converting a general transcription factor into an operon-specific virulence regulator. Mol. Cell 26, 117–129 (2007). [PubMed: 17434131]

41. Molodtsov V, Sineva E, Zhang L, Huang X, Cashel M, Ades S, and Murakami K Allosteric effector ppGpp potentiates the inhibition of transcript initiation by DksA. Mol. Cell 69, 828–839 (2018). [PubMed: 29478808]

42. Artsimovitch I, and Landick R Pausing by bacterial RNA polymerase is mediated by mechanistically distinct classes of signals. Proc. Natl. Acad. Sci. USA 97, 7090–709 (2000). [PubMed: 10860976]

43. Sambrook J, Fritsch E and Maniatis T Molecular Cloning: A Laboratory Manual (Cold Spring Harbor Laboratory, Cold Spring Harbor, NY) (1989).

44. Suloway C, Pulokas J, Fellmann D, Cheng A, Guerra F, Quispe J, Stagg S, Potter C, and Carragher B Automated molecular microscopy: the new Leginon system. J. Struct. Biol 151, 41–60 (2005). [PubMed: 15890530]

45. Zheng S, Palovcak E, Armache J, Verba K, Cheng Y, Agard D MotionCor2: anisotropic correction of beam-induced motion for improved cryo-electron microscopy. Nature Meths. 14, 331–333 (2017).

46. Rohou A and Grigorieff N CTFFIND4: Fast and accurate defocus estimation from electron micrographs. J. Struct. Biol 192, 216–221 (2015). [PubMed: 26278980]

47. Zivanov J, Nakane T, Forsberg B, Kimanius D, Hagen W, Lindahl E, Scheres S New tools for automated high-resolution cryo-EM structure determination in RELION-3. eLife 7, e42166 (2018). [PubMed: 30412051]

48. Pettersen E, Goddard T, Huang C, Couch G, Greenblatt D, Meng E and Ferrin T UCSF chimera - a visualization system for exploratory research and analysis. J. Comp. Chem 25, 1605–1612 (2004). [PubMed: 15264254]

49. Emsley P, Lohkamp B, Scott W and Cowtan K Features and development of Coot. Acta Cryst. D 66, 486–501 (2010). [PubMed: 20383002]

50. Afonine T, Headd J, Terwilliger T and Adams P Computational Crystallography Newsletter 4, 43–44 (http://phenix-online.org/newsletter/CCN_2013_07.pdf) (2013).

51. Mastronarde D Advanced data acquisition from electron microscopes with SerialEM. Microsc. Microanal 24. 864–65 (2018).
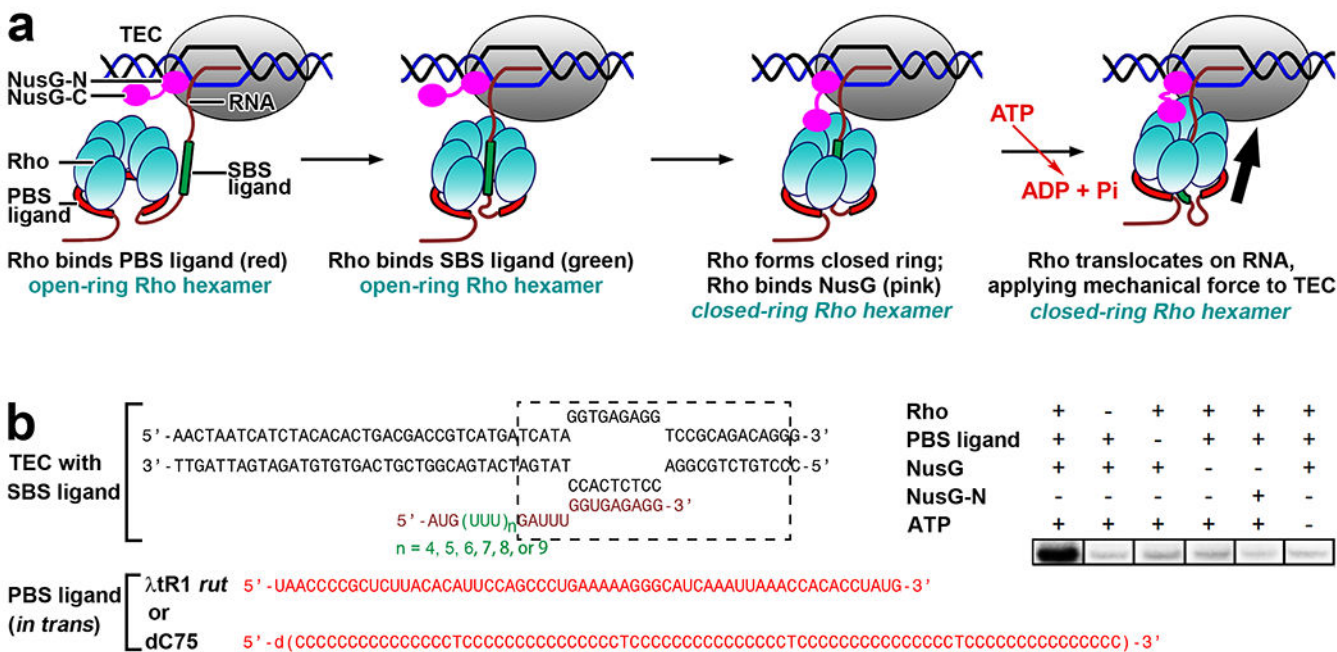
Fig. 1. Rho-dependent termination

(a) Proposed mechanism of Rho-dependent termination[1–4]. In first step (image 1), the Rho hexamer in an open-ring state--either free or in complex with a TEC-- recognizes a long C-rich RNA sequence (PBS ligand; also known as *rut* site) through a primary binding site (PBS) on the exterior of the Rho hexamer (image 1). In second step, the Rho hexamer in an open-ring state recognizes a short pyrimidine-rich RNA sequence (SBS ligand) through a secondary binding site (SBS) in the central channel of the Rho hexamer (image 2). In third step, the Rho hexamer transitions from the catalytically inactive, open-ring state to the catalytically competent, closed-ring state; this reaction is facilitated by interactions with NusG (image 3). In fourth step, the Rho hexamer in the catalytically active, closed-ring state performs ATP-dependent 5'→3' translocation on RNA toward the TEC, exerting mechanical force on, and disrupting, the TEC (image 4). Rho, cyan; RNAP in TEC, gray; nontemplate-strand DNA, template-strand DNA, and RNA, black, blue, and brick-red, respectively; PBS ligand, red; SBS ligand, green; RNA 5' to PBS ligand, RNA between PBS ligand and SBS ligand, and spacer RNA between SBS ligand and TEC, brick-red; NusG, magenta.

(b) Scaffold assay for Rho-dependent termination. Left, nucleic-acid scaffolds comprising: (i) determinants for formation of a TEC (nontemplate- and template-strand DNA oligomers in black, and RNA oligomer in brick-red and green; boundaries of TEC denoted by dashed rectangle); (ii) 5' extension of RNA oligomer containing 4, 5, 6, 7, 8, or 9 codons of U-tract RNA as SBS ligand; and (iii) RNA oligomer carrying λtR1 *rut* site (red) or dC75[22] (red), provided *in trans*, as PBS ligand. Right, RNA-release data showing that scaffold with λtR1 *rut* site provided *in trans* is functional in Rho-dependent termination. Assays were performed twice with consistent results.
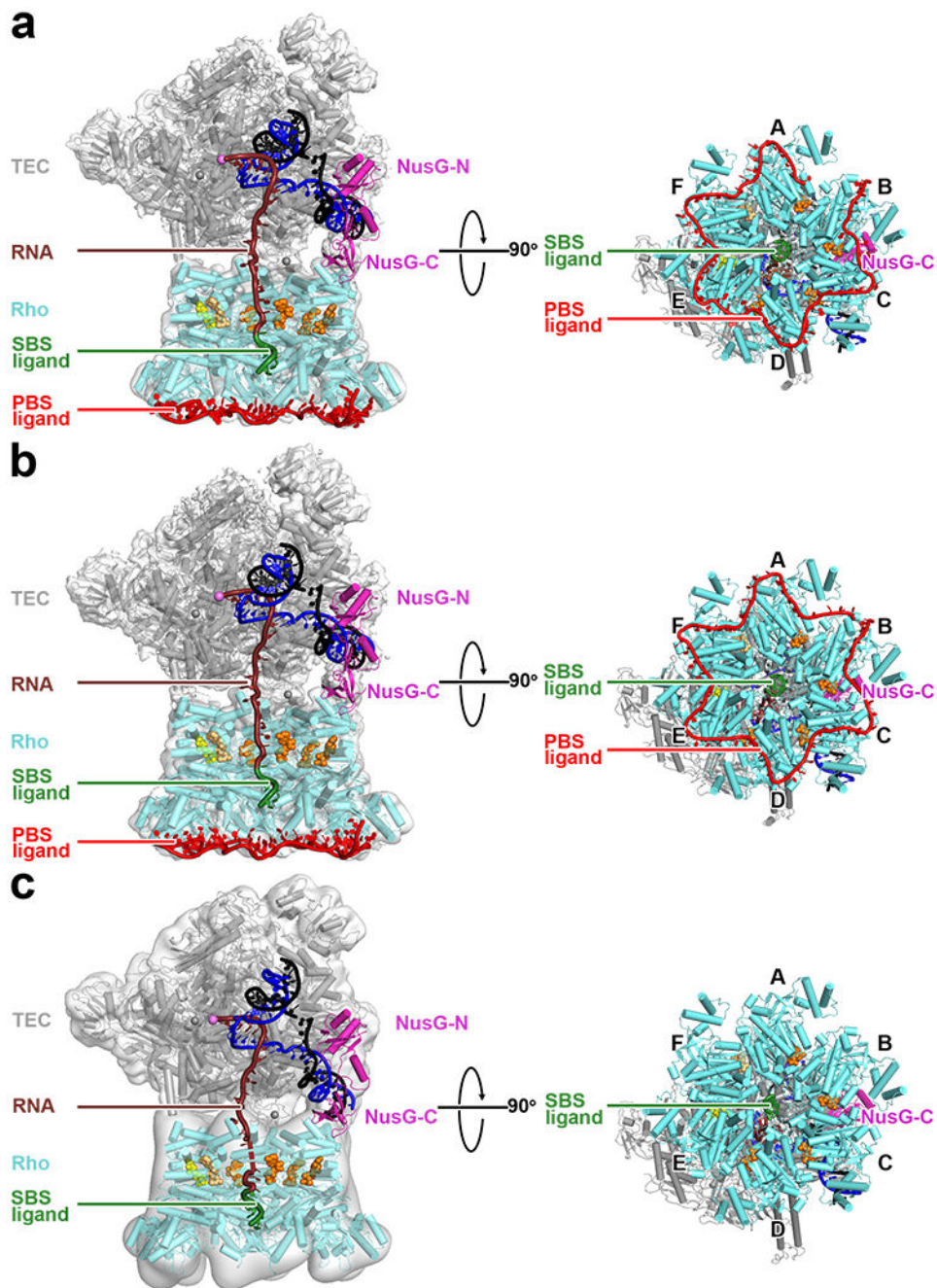
Fig. 2. Structures of Rho pre-termination complexes

(a) Structure of complex with λtR1 *rut* RNA provided *in trans* as PBS ligand (λtR1-Rho-NusG-TEC).

(b) Structure of complex with dC75 *rut* RNA provided *in trans* as PBS ligand (dC75-Rho-NusG-TEC).

(c) Structure of complex with no PBS ligand (Rho-NusG-TEC).

Left panels, view orientation having Rho-hexamer central channel aligned with y-axis, showing passage of RNA through TEC RNA-exit channel and through Rho-hexamer central
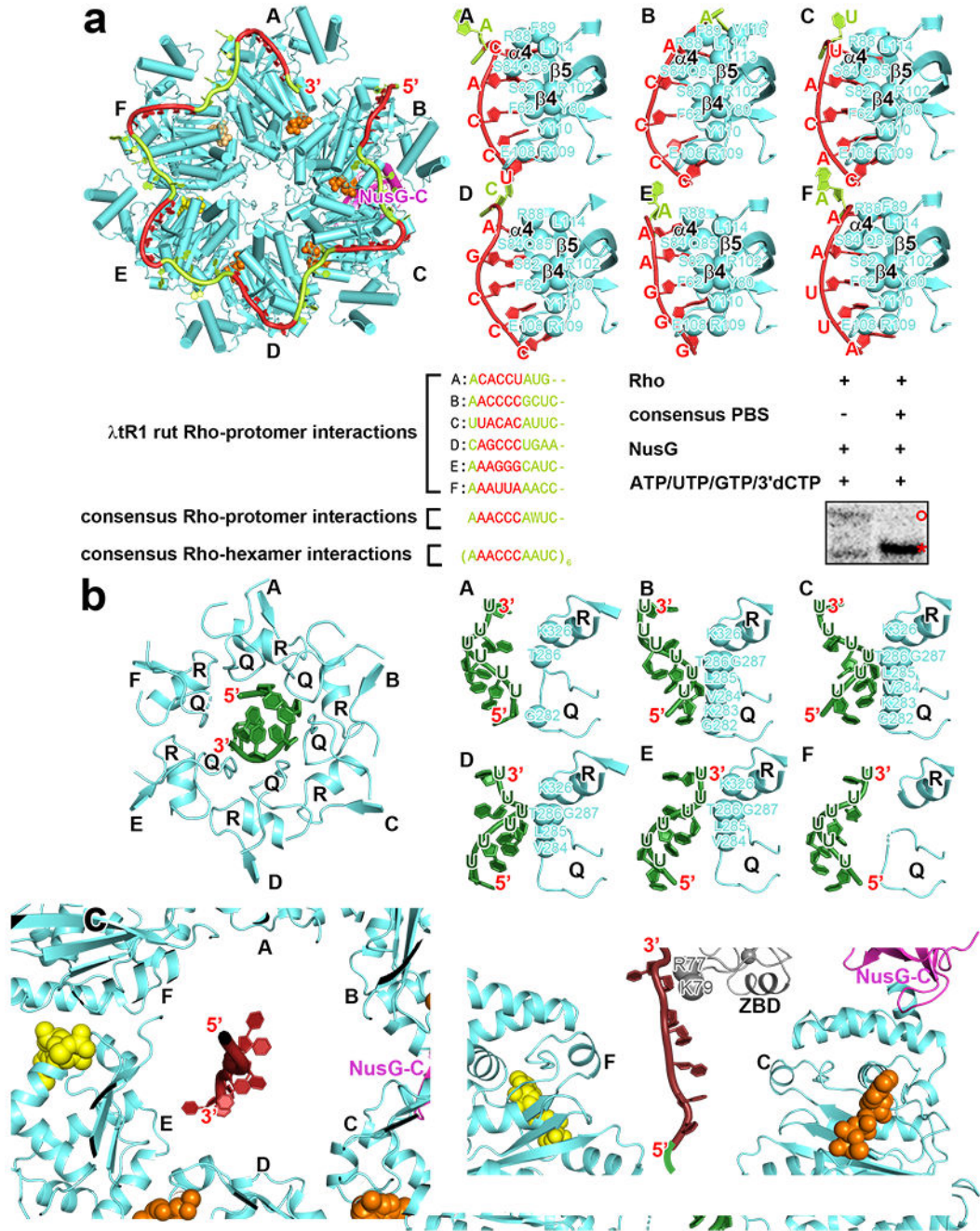
channel. Right panels, orthogonal view orientation showing interaction of PBS ligand with Rho protomers A-F. Mg-ADP-BeF$_3$ molecules, orange surfaces (high occupancy), light orange surfaces (low occupancy), and yellow surfaces (very low occupancy). Other colors as in Fig. 1a.

Fig. 3. Protein-RNA interactions in Rho pre-termination complex

(**a**) Protein-RNA interactions by Rho PBS. Upper left, overall interaction (contacted nucleotides, red; non-contacted nucleotides, light green; view orientation and other colors as in Fig. 2, right). Upper right, details of interactions for Rho protomers A-F, Rho residues that interact with PBS ligand RNA are shown as cyan spheres. Lower left, 10 nt PBS-ligand sequences contacted by Rho protomers A, B, C, D, E, and F in λtR1-Rho-NusG-TEC, 10 nt inferred PBS-ligand consensus sequence for Rho protomer interaction, and 60 nt inferred PBS-ligand consensus sequence for Rho hexamer interaction, colors as in A. Lower

right, RNA-extension data showing that an RNA oligomer carrying the inferred PBS-ligand consensus sequence is functional in Rho-dependent termination. Assays were performed twice with consistent results.

(b) Protein-RNA interactions by Rho SBS. Left, overall interaction, focusing on 6 nt SBS ligand (green) and structural elements of Rho that interact with SBS ligand (Q-loop and R-loop) (view orientation and other colors as in Fig. 2, right). Right, details of interactions of Rho protomers A, B, C, D, E, and F.

(c) Protein-RNA interactions with spacer RNA between Rho SBS and TEC. Left, overall interaction, showing large distances, and absence of contacts, between Rho and spacer RNA (view orientation and colors as in Fig. 2, right; SBS ligand and Rho structural elements that interact with SBS ligand omitted for clarity). Right, orthogonal view, showing large distances, and absence of contacts, between Rho (protomers A-B and D-E omitted for clarity) and RNA, and showing interactions of 2 nt of spacer RNA with RNAP β'-subunit ZBD.
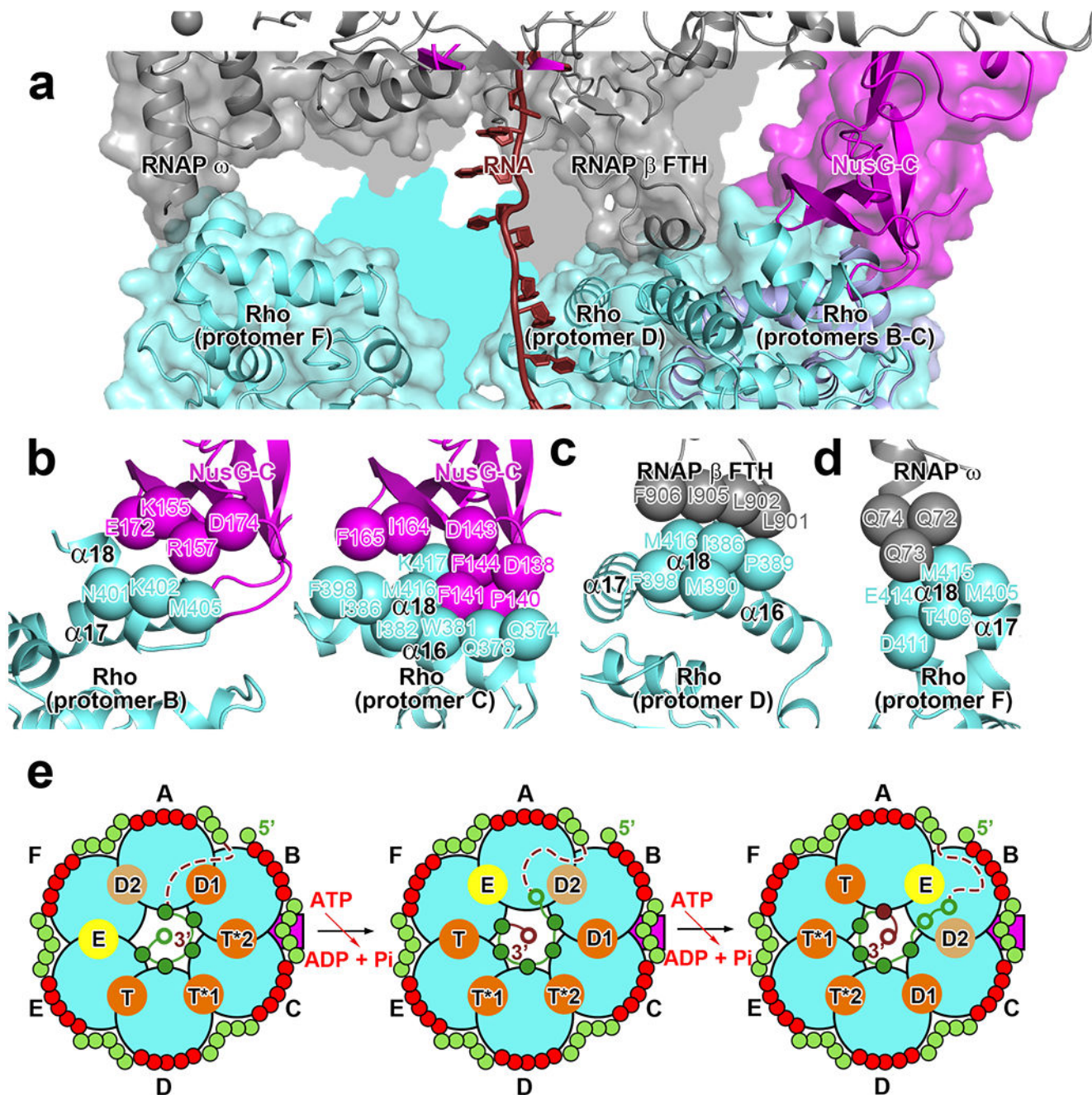
Fig. 4. Rho-TEC interactions and ATP-binding-site motor states in Rho pre-termination complex

(a) Interface between Rho and NusG-containing TEC in λtR1-Rho-NusG-TEC (view orientation and colors as in Fig. 2, left).

(b) Protein-protein interactions between Rho protomers B (left) and C (right) and NusG-C.

(c) Protein-protein interactions between Rho protomer D and RNAP β-subunit FTH.

(d) Protein-protein interactions between Rho protomer F and RNAP ω subunit.

(e) Motor states of Rho ATP binding sites in Rho pre-termination complex (left), inferred motor states after first step of Rho-dependent ATP hydrolysis (center), and inferred motor

states after second step of Rho-dependent ATP hydrolysis (right). Motor states are as follows: the ATP binding state (T), pre-catalysis ATP-bound state (T*1), catalytically competent ATP-bound state (T*2), ADP-bound state 1 (D1), ADP-bound state 2 (D2), and nucleotide exchange state (E)[4,22]. View orientation and colors as in Fig. 3a. PBS-ligand nucleotides, red circles for contact residues and light green circles for non-contact residues; SBS-ligand nucleotides, green circles (filled circles when interacting with SBS; open circles when not); spacer-RNA nucleotides, brick red circles (filled circles when interacting with SBS; open circles when not); orange, light orange, and yellow filled circles, Rho ATP binding sites (high-occupancy, low-occupancy, and very-low-occupancy ATP binding sites, respectively); magenta, NusG-C; curved black dashed lines, RNA connecting 3' end of PBS ligand to 5' end of SBS ligand.